STUDY OF MRK 110 USING X-RAY SPECTROSCOPY

by

Xiao (Jennifer) Liang

A thesis submitted in partial fulfillment
of the requirements for the degree

of

Master of Science

in

Physics

MONTANA STATE UNIVERSITY
Bozeman, Montana

May 2019

ACKNOWLEDGEMENTS

I would like to express my gratitude to Dr. Anne Lohfink, Dr. Charles Kankelborg, and Dr. Gregory Francis for being on my committee and reading my thesis. I would also like to thank Montana State University for providing me an opportunity to study physics at the graduate level. Special thanks to Professor Lohfink for working with me on this project. This has helped me to learn a lot about myself as well as the subject matter.

Next I would like to thank the friends and teachers who have helped me in my journey to pursue a master's degree. I want to thank them for supporting me during some of the most difficult times while showing me how to hold on to my dream of contributing to science.

TABLE OF CONTENTS

LIST OF FIGURES

LIST OF FIGURES – CONTINUED

LIST OF FIGURES – CONTINUED

LIST OF FIGURES – CONTINUED

NOMENCLATURE

AGN	Active Galactic Nuclei
SMBHs	Super Massive Black Holes
Hardening	Flux of Higher energy photons are detected
Softening	Flux of Lower energy photons are detected
XRTE	Rossi X-ray Timing Explorer
NuSTAR	Nuclear Spectroscopic Telescope Array (observatory)
SWIFT	The Neil Gehrels Swift Observatory

ABSTRACT

Jets are one of the most mysterious, and fascinating subjects in the study of relativistic outflow of the high energy particles produced by the Active Galactic Nuclei (AGN). AGNs are the center of active galaxies, where a very massive black hole is actively accreting matter into it. The relationship between the black hole mass and the luminosity is produced through accretion is known as the fundamental plane of black hole activities. The goal is to probe the characteristics of the black hole and its close vicinity by studying the X-ray produced by this inner region.

We report the finding of high energy X-ray photons of a low radio luminous galaxy Mrk 110 from NuSTAR observations.

We've found there are almost no variations in the X-ray flux during time scale observation, and there is a linear correlation between 3-5 keV and 5-10 keV energy band. We also find that the energy spectrum is best modeled by a cutoff power law and a red-shifted Gaussian modeling the fluorescence emission. Fluorescence emission is one of the signatures when X-rays are reflected by the disk. However the other significant reflection component, –X-rays signals reflected by the disk, is missing. We suspect the cause of the unexpected amount of high energy X-ray flux is due to jet emissions.

1

INTRODUCTION

"The nitrogen in our DNA, the calcium in our teeth, the iron in our blood, the carbon in our apple pies were made in the interiors of collapsing stars. We are made of star stuff."

–Carl Sagan

The early universe only consisted of hydrogen, helium, and a very small amount of lithium. The first stars were formed from the gravitational collapse of those elementary gases. Inside the star, the fusion process creates most of the heavier elements we see today. When the stars die, they blow out all of the heavier elements they made into their surrounding gaseous environments. From there the process repeats itself: the gaseous environments condense into stars again. The gas and element rich environment that promotes the star formation process is known as the Interstellar Medium (ISM). The ISM is an accumulation of remnants from dying stars that has spread between the star systems in a galaxy. Galaxies, which the ancients named due to their "milky" appearance, are defined as a collection of ISM and stars.

Galaxies are mainly classified into three types: spiral(Fig 1.1), and irregular(Fig 1.2),elliptical(Fig 1.3). Spirals galaxies are disk like galaxies and typically have a spiral-like appearance. They are still rich in gas and star formations. Elliptical galaxies are spheroidal shaped. They are typically old and have exhausted all of their gas for star formation. Finally Irregular galaxies, as their name suggests, do not have easily classified shapes. They are the result of two galaxies that have merged or are in the process of merging.

Figure 1.1: Spiral galaxies are gas and dust rich, and contain spiral arms which are favored for star formation. (Subaru Telescope (NAOJ), Hubble Space-Telescope, European Southern Observatory)

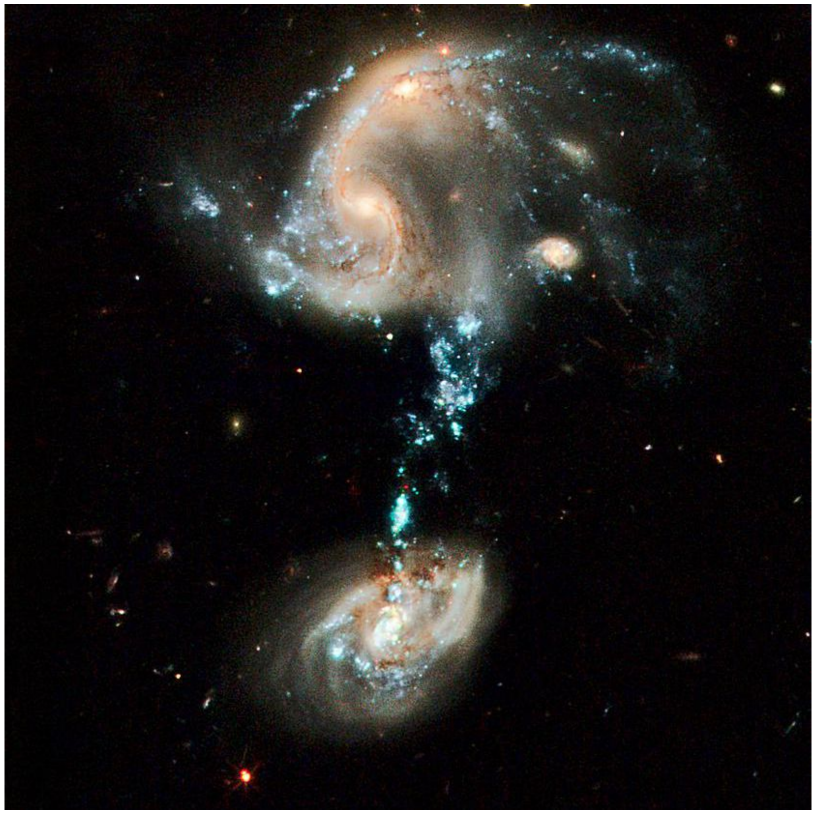

Figure 1.2: Irregular galaxies have an irregular shape due to collision with other galaxies. They are also rich in gases with active in star formations (NASA/ESA/STScI)

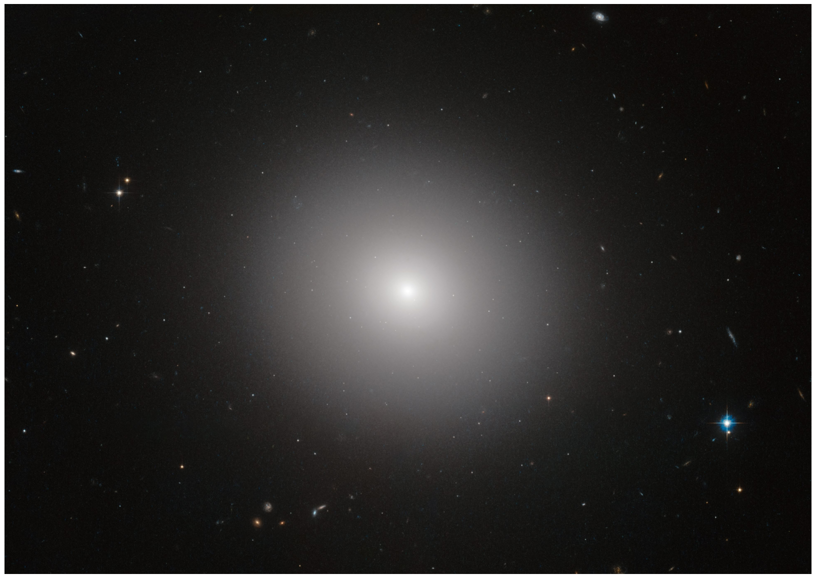

Figure 1.3: Elliptical galaxies are spheroidal in shape, they do not contain as much gas or dust, and the stars are typically old and have lower mass (NASA/ESA/Hubble Image)

Despite their differences, all three galactic types share a common feature : they all have a very bright center. Early astronomers suspected the bright center region consisted of a large number of stars, but the radius of the most luminous region is only about 100 parsecs (1 parsec is 3.26 light years). This suggests a mass of a few 10^8 solar masses must be concentrated in this region. A very massive, actively accreting star was proposed to explain the broadening of the emission lines from this region.

However, temperature observations from this region contradicted this mode. Studies from Morris in 1983 and Hüttemeister in 1993 demonstrated that the gas temperatures in the center of Milky Way can be as hot as 200 Kelvin. This would make the gas too hot to collapse from its own gravitational pull and form stars.

The spectrum from the central region shows that the galactic center is radiating photons with energy higher than those from the stars. There is a significant broadening of the spectra emitted from this region, which suggests a high velocity of the radiating material. In order to account for these discrepancies, the super massive black hole (SMBH) accretion disk model was put forth as a better explanation [5]. The SMBH model was proposed by Salpeter in 1964 and Lynden-Bell in 1969 because it better explained the energy output and variability seen from the bright galactic centers.However, not all galaxies have an accreting black hole residing at the center. The galaxies that contain a black hole actively accreting materials are called active galaxies. The active black hole accreting regions are called Active Galactic Nuclei (AGNs).

AGN sometimes produce a powerful outflow of ionized matter called jets. Sometime those jets accelerate matter to near the speed of light, and those jets became relativistic. But not all AGN have jets outflow, and the formation of the jets are still unknown.

Jets are found to have very strong (loud) radio signal. It is believed that the radio waves are produced by the jets through synchrotron radiation, a process by which an electron emits a radio wavelength photon. Therefore, radio loud AGN suggest a strong jet out flow. There are certain AGN that have lower or no radio signals. These are called radio quiet AGNs.Studies have shown that those AGNs are also active and possibly produce jets, but the jets are suppressed by some kind of mechanism.

AGN are comprised of a SMBH, an accretion disk, a corona and a dusty torus. The dusty torus is made up of clouds of $1\ \mu$m molecules that are located farther out from the active accretion region. The SMBH resides at the center of AGN and is actively accreting gas from the surrounding environment. This forms a hot disk of gas around the SMBH. The corona consists of a plasma cloud of H and He atoms close to the most inner region of the black hole.

The goal of studying radio quiet galaxies is to understand the abnormal jet activities. The earliest radio quiet galaxies discovered were the Seyfert galaxies. They are mainly categorized into Type I and Type II depending on the emission lines in their spectra. Type I galaxies typically show both broad emission lines (e.g. H,He) and narrower lines due to electron transitions normally not allowed by the quantum selection rules (these are known as the forbidden lines). Type II Seyfert, on the other hand, only show narrow lines in both the forbidden lines and allowed transitions. The studies from Antonucci, Miller [3] and Unger [43] suggest that the difference between Seyfert I and II galaxies are the viewing angles. Seyfert I galaxies expose the black hole and accretion disk for direct observation, and Seyfert II galaxies are the viewed through the planes of the AGN (see in Figure 1.5). We can also distinguish the difference between the two types of Seyferts via their X-ray intrinsic absorption measurement. Typically, lower energy X-rays (E<< 5 keV) are absorbed in a region close to the black hole. The measurement of the absorption is called column density of hydrogen N_H, it has units of atoms per cm^2.

Seyfert II galaxies have strong absorption density, due to the more absorbing material in the line of sight. it is chosen that $N_H > 10^{22} cm^{-2}$ are optical Seyfert II galaxies, and $N_H < 10^{22} cm^{-2}$ are Seyfert I galaxies [6].

Seyfert I galaxies present a direct view into the central region of the AGNs, and less X-rays will be absorbed due to interference (Fig 1.4). This allows us to peek into the central engine and physical processes very near to the black hole. This makes them a better candidate to study the central region processes.

The AGN is very small compared to its host galaxy. The AGN vicinity we studied in this thesis was about 0.1-10 pc across [22], compared to the galaxy diameter of 30 kpc [46]. Despite the small size of AGN, recent study has shown that AGNs may play a crucial role in the galaxy formation. Specifically, it may help determine the gas exhaust rate in a galaxy. This indirectly influences the galaxy mass and star formation rate (SFR).

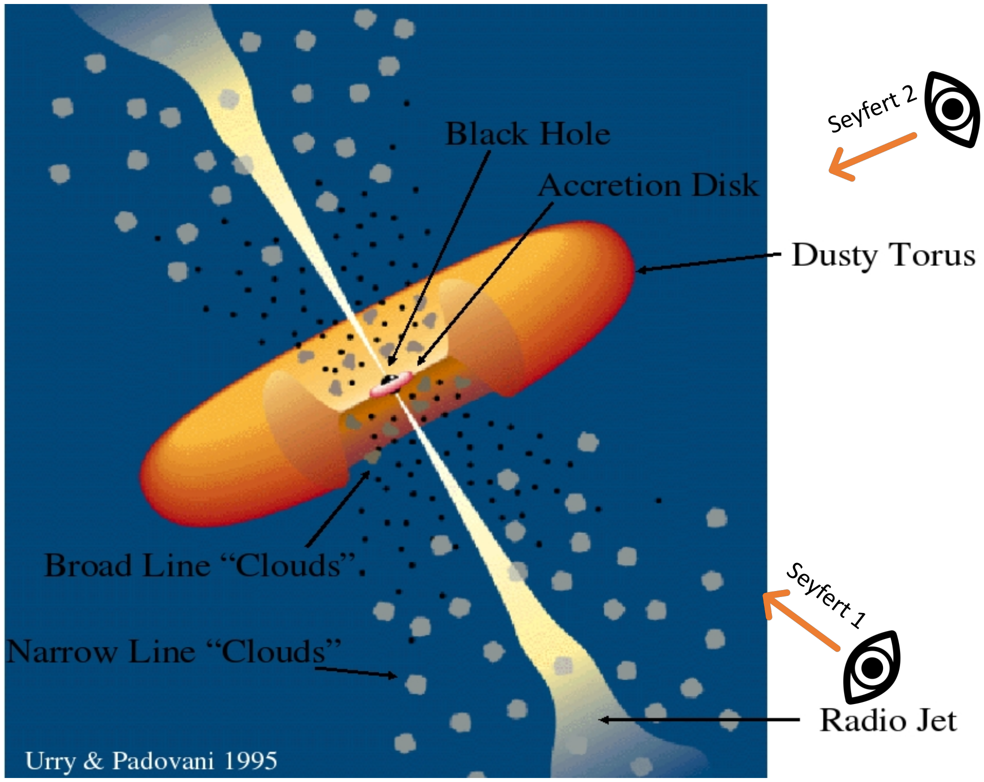

Figure 1.4: Structure of AGN consists of a SMBH, an accretion disk, and thick dust clouds (sometime in a torus shape). The difference between Seyfert I and Seyfert II galaxies is the plane of view of AGN. Note the torus and Central AGN drawn here are not to scale (picture credit to [10])

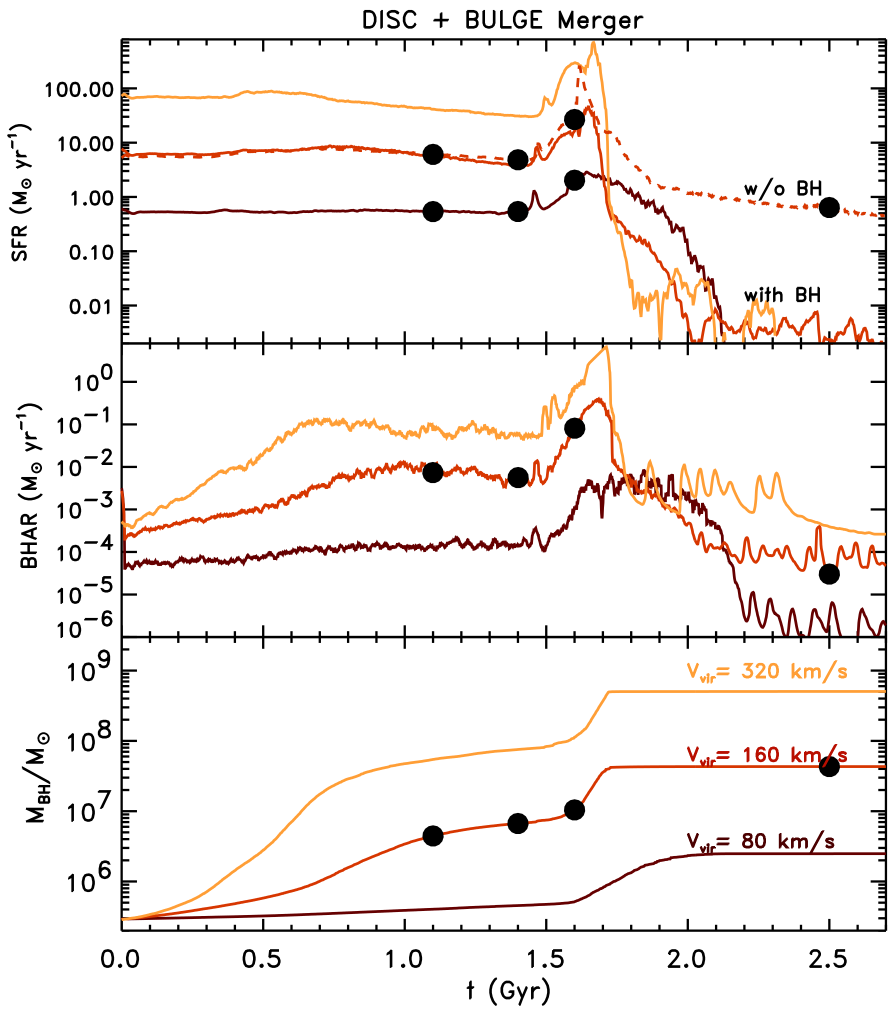

Figure 1.5: A modeled result of the black hole mass correlations to the star formation rate, black hole accretion rate, and black hole mass, for a two black hole merging event between two galaxies each with black hole mass equivalent to Milky way scale galaxies. (Plot Credit: [11])

Fig 1.5 shows the simulated SFR, SMBH accretion rate, and SMBH masses for two galaxies that merged together. The top panel suggests that, shortly after the merger, a large amount of star formation was induced. The merger with the highest black hole mass and accretion rate terminates SFR in 0.2 Gyrs while the merger with the lower mass and lower accretion rate terminates SFR in 0.5 Gyrs. Galaxy mergers without any black holes have a constant SFR [11].The mechanism of how an AGN influences the host galaxy is known as the galactic feedback process.

As of today's study, it is believed that AGN influence the galaxy through jets and outflow wind. The production mechanism of jets and galactic outflow is still unclear. But we are not completely clueless on the relationship between all of the components of AGN. Studies from Merloni and his team found there are correlations between the jet power (in the form of radio signal), accretion disk power (in the form of X-ray emission), and mass of the SMBH. [35].

The relationship shown in Fig 1.6 is known as the Fundamental Plane for accreting black holes. L_R is the measured radio luminosity, L_X is the X-ray luminosity, and M is the black hole mass. This plot shows all three quantities and follows a linear relationship on a log-log scale. Therefore, if we study the radio and X-ray components of the AGN, we can deduce the black hole mass at the center of the AGN.

The black hole only has three associated quantities: mass, angular momentum (or spin), and electric charge. The fundamental plane of accreting black hole gives us a possibility to probe the black hole mass from observing radio and X-ray luminosity. But the X-ray luminosity and flux gives us more information about the inner region of the AGN vicinity and the black hole itself. From decades of study it has become evident that X-rays come from the compact accretion region. The X-rays originate from a region that is very close to the SMBH. Therefore, it acts as a powerful tool for us to study the environment that is close to the black hole and the accretion

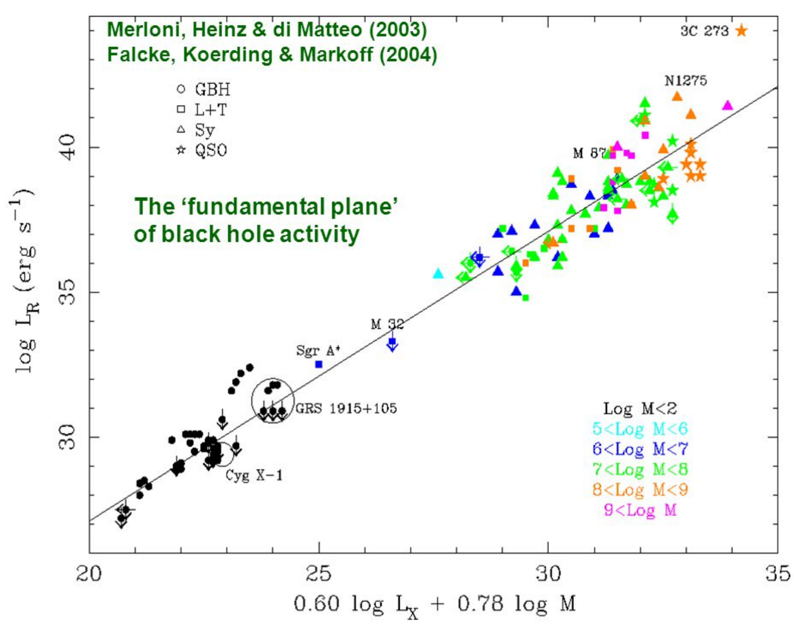

Figure 1.6: The plot shows the relationship between Radio luminosity (L_R), X-ray luminosity (L_X), and the mass of a black hole (M), where they fall onto a linear fitting line on a log-log scale. This known as the black hole fundamental plane [35].

disk. Although we can't directly resolve this close region to the SMBH, we are able to analyze and infer the physical processes in the vicinity via timing analysis and spectroscopy.

In order to detect X-rays, we need to place the observatory above our atmosphere. X-rays have high energy and very short wavelength. Thus, X-ray photons cannot be focused with a normal incident mirror, due to X-ray's index of refraction on any material being only slightly smaller than 1. This means a small angle of incidence gives very sufficient reflection.

However, if the incident angle is too large X-rays will be absorbed by the material or will be scattered into unintended directions. In order to collect X-rays, the mirror must be oriented along the direction of travel, and the X-rays are focused by a parabolic mirror and then a hyperbolic mirror, show in Fig 1.8 and Fig 1.9. This method of X-ray detection is used in many high resolution X-ray telescopes. Each telescope can be configured to detect a certain energy range of X-rays.

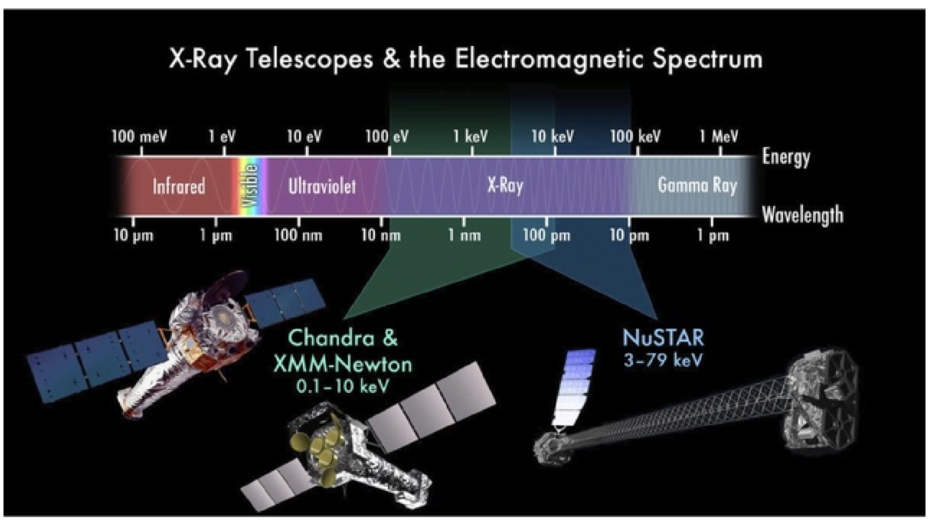

Figure 1.7: X-ray detectors listed with their corresponding to detection range [8]

In this project, we have analyzed data from NuSTAR observatory. The NuSTAR space telescope was launched on June 13, 2012, and it can detect X-rays in the 3.-79keV range. The long extension of the NuSTAR observatory is necessary because the focusing mechanism requires a long distance.

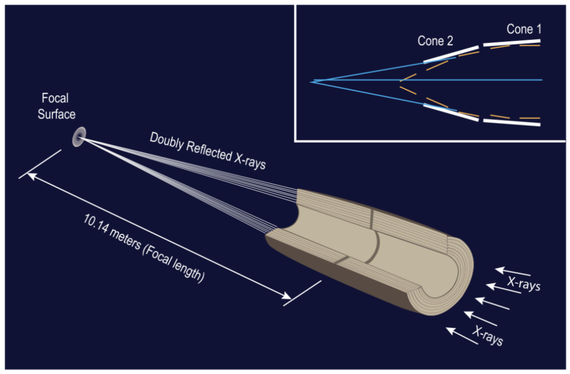

Figure 1.8: The NuSTAR focus mechanism consists of two sections of mirrors, which allows the X-ray to focus at 10.14 meters away [38]

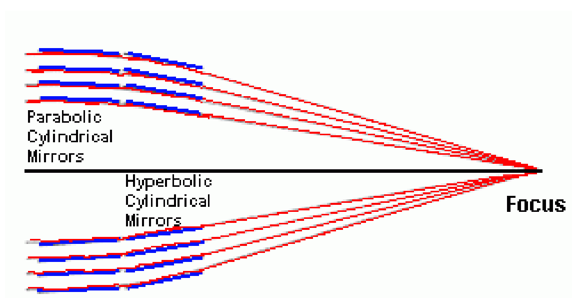

Figure 1.9: X-rays come in with a very small incident angle, grazing the mirror and deflecting X-rays to focus them [12].

The focused X-rays are collected by the solid state photon counting detector modules (FPM A & B), where each of the modules are 32 $\times$ 32 pixels [28]. Each of the pixels will record the count of photons, energy of photons, x received position (+x is down), y position received position (+y is left), and error of counting. For example Fig 1.10 shows a signal view on the detector models.

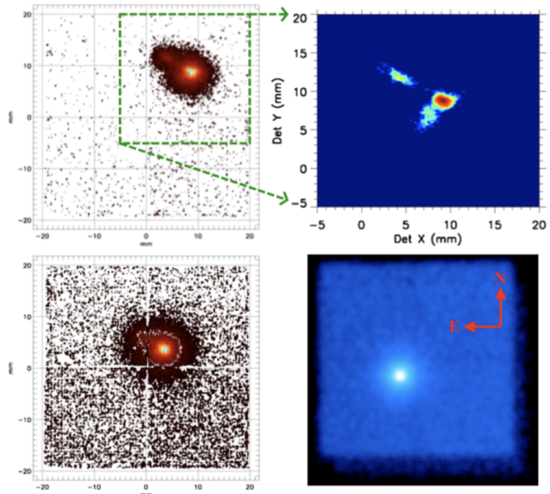

Figure 1.10: X-ray image of Fairall 9. Top left is the image of a 49 kilo-seconds(ks) exposure. Lower left panel shows a 94 ks exposure after refining the grid alignment. Lower right panel shows the sky image of the same object [28].

We are mostly interested in understanding the relationship between the counting rate and its corresponding energy. The counting rate is the X-ray flux we received at the detector. The energy distribution corresponds to the amount of counts received and gives information about the source that produced them. If we plot the spectrum corresponding to their energy level, we would obtain a plot similar to Fig 1.11. The goal is to fit the data with a modeled curve. The physical meaning of the fitting components used to construct the curve and fit the data will be given in the Chapter 2.

The tool we employed to fit the data is Xspec. It is a command based interactive X-ray fitting program [27]. Users are able to crop and ignore bad data contributions from detector noise and conducting binning to process the raw data. The desired model that best fits the data can then be selected (power-law, red-shifted Gaussian, etc). The values returned from each component of the parameters have physical significance for understanding the AGN environment.

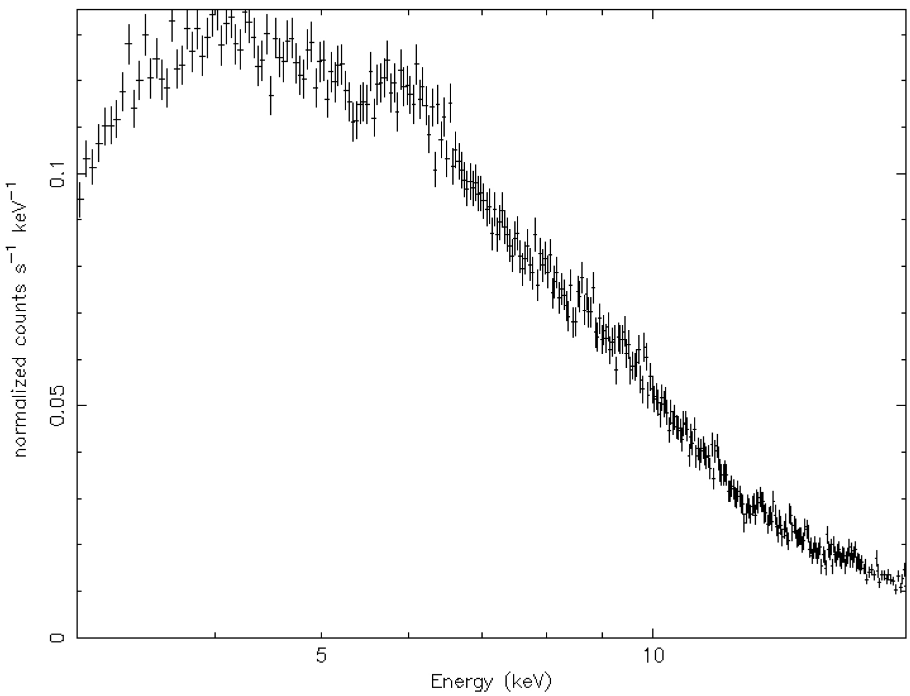

Figure 1.11: Data plot normalized the count rate respective to the energy in keV(kilo-electron volt). This is a raw data plotted from NuSTAR , FPM A detector for a total exposure time of 17.8 ks

Guide

In this thesis, I will focus on the study of a particular Seyfert I galaxy named Mrk 110. This source has a behavior which seems to contradict the fundamental plane of accreting black holes. Mrk 110 has been observed to have the same amount of accretion rate and black hole mass as the radio galaxy 3C 120. However, Mrk 110 has a radio luminosity 3 times lower compared to 3C 120 [9].

The suppressed radio flux makes Mrk 110 a particular point of interest. We wish to understand if the X-ray flux from Mrk 110 will provide a deeper insight into the cause of the radio flux differences. We also wish to determine the crucial conditions that affect jet production efficiency.

In the following chapter, I will illustrate the structure and components of an AGN. Then I will examine the physical meaning of the signatures we observed in the data and modeling in the spectroscopy chapter. Following that, I will discuss in detail how we conducted the analysis in the methods section. Finally, the results found for Mrk 110, and our interpretation of these results, will be discussed.

STRUCTURE OF AGN AND X-RAY SPECTROSCOPY

AGN

In an active galaxy the AGN is the brightest part of the galaxies and resides at the center. We know the brightness is not completely due to the star formation, when we inspect the spectrum from the AGN we find spectra that is not produced by stars. Stars radiate photons which obeys black body radiation, but the spectrum observed from AGN suggests that the radiation process is not thermal, but is described by power law. These kinds of phenomenal are only possible through Compton scattering or synchrotron radiation [2], which suggest high energetic processes must be occurring within the central vicinity.

In the introduction I briefly described the structure of AGN. It consists of a SMBH, an accretion disk, and a high temperature plasma corona surrounded by dust clouds/torus (see Fig 1.4). The dusty torus is located around 100 pc [42], but we are most interested in a much smaller vicinity around the black hole. The majority of the high energy physical processes are within the region of 0.1-10 pc, which mainly includes the SMBH, accretion disk, and the Corona. The accretion disk are estimated to be about 0.1 pc or about 10 light years across ([22]).

Accretion disk

The accretion disk model mentioned in this thesis are assumed to be geometrically thin, but optically thick (meaning it is thin in the vertical extension), but it is very dense and reflects very well. The accretion disk produces the primary photons which later will be scattered into X-rays in the AGN region. The accretion disk is formed by hot gas spiraling into the SMBH, but during the initial spiral processes, the angular momentum of the matter prevents them from falling directly into the black hole. However, the gas and matter in the accretion disk can't flow without experiencing friction and resistance, thus the friction from the viscosity will heat up the gas, and energy is carried away in the form of radiation. This process produces thermal photons as a thermal radiating process, which is the radiation produced by the accretion disk.

If we assume the disk is releasing gravitational energy at rate of $\frac{\mathrm{GM\dot{M}}}{\mathrm{r}}$, then we apply the virial theorem, which says that $2 < KE >=< PE >$ (In this case we only considered the energy magnitude), then the temperature of the accretion disk around the SMBH is given by $T \propto (M\dot{M})^{1/4}r^{-3/4}$. M is the mass of the SMBH, $\dot{M}$ is the amount of mass accreted by the black hole, R is the radius of the accretion disk measured from the center of rotation. We can see from this equation, it predicts that a larger mass black hole has an accretion disk with a cooler temperature, due to a larger mass black hole having a greater Schwarzschild radius (the radius of the black hole where the escape speed is equals to the speed of light). Therefore, the highest temperature of the disk is in the most inner region, and at the most inner region of the SMBH, the disk radiates at the UV spectrum, the outer parts of the accretion disk is radiates with optical light, and infrared.

The temperature cools as the disk radius increases. Each part of the disk produces a black-body spectrum, therefore we can find the total flux contributed from each black-body curve by integrating the black body curve with the disk area. And the resulting spectrum for the disk is shown in Fig 2.2.

The disk spectrum is the source of photon distribution, which are scattered into the X-ray spectrum. The emission from accretion disk only produces a very minimal amount of X-rays (Due to black-body radiation), the amount of X-rays produced by this procedure is not likely to be observed at all. Something else must be producing the amount of X-rays we observed. The photons are created by the disk, but those

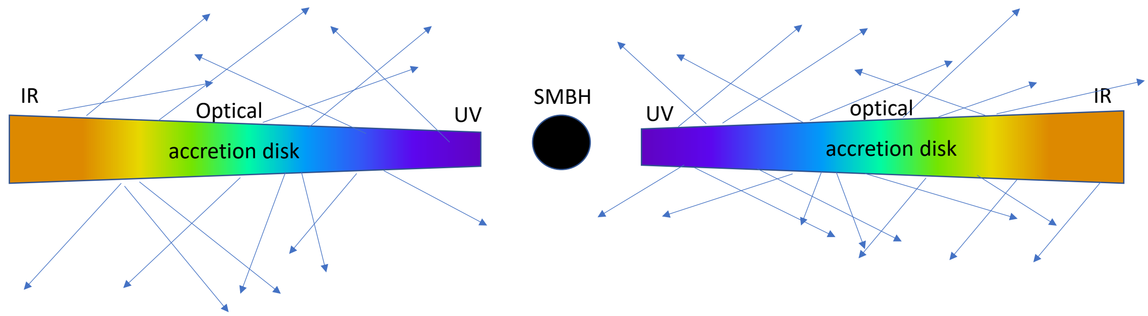

Figure 2.1: A cut through side of an accretion disk and the super-massive-black hole. The disk is colored to represent the temperature gradient, but its not to an accurate scale (e.g. the purple region represents UV emission, and the orange represents infrared emission). Arrows represent photons emission in all directions.

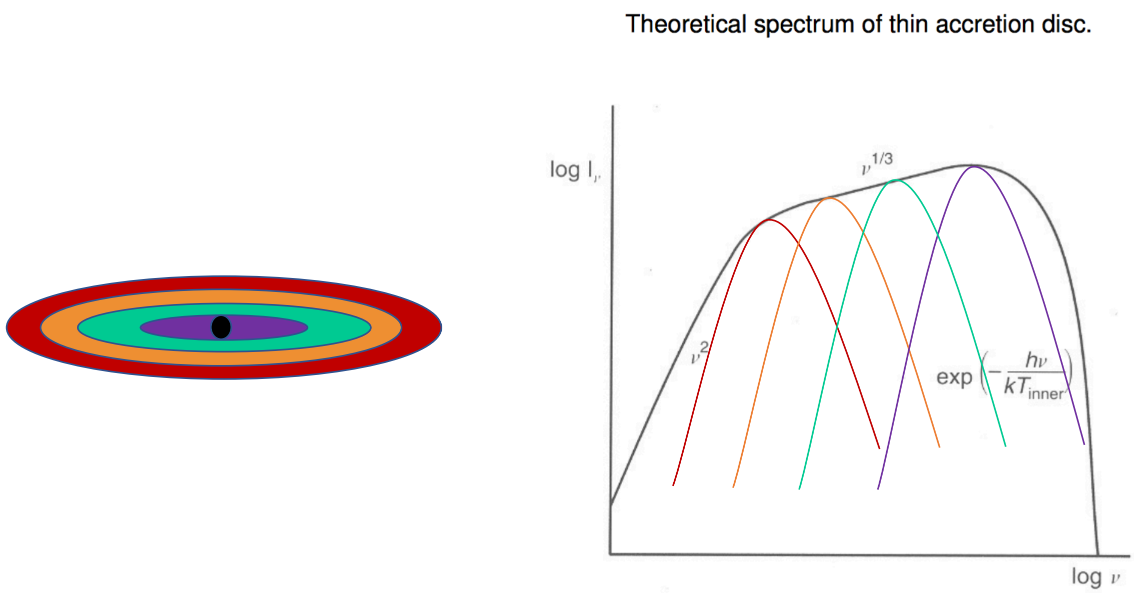

Figure 2.2: The net disk spectrum from integrating the Black-body curve and the radius of the disk. The lower temperature black-body spectrum is red, indicating the outer parts of the disk. Orange and green indicate the center part of the disk, which is added to the spectrum. The innermost part of the disk contributes to the highest energy band of the total spectrum [26].

photons are scattered into X-rays by the ionized plasma, which is called the accretion disk corona.

Corona

The accretion disk corona is very different from the solar corona. We are not exactly sure the location and the mechanism of formation to the corona, but we know the corona is made of plasma from the ionized H and He. There are currently two theories on how the corona is distributed. One of the models is the lamppost model (shown in Fig 2.3). The other is called the “sandwich” model (shown in Fig 2.4). In both case the accretion disk emits photons in all directions, and the photons will be captured by the corona, and be scattered by the Inverse-Compton scattering process. A recent study from [18] have shown suggest that the lamppost model is a more suitable model for the AGN.

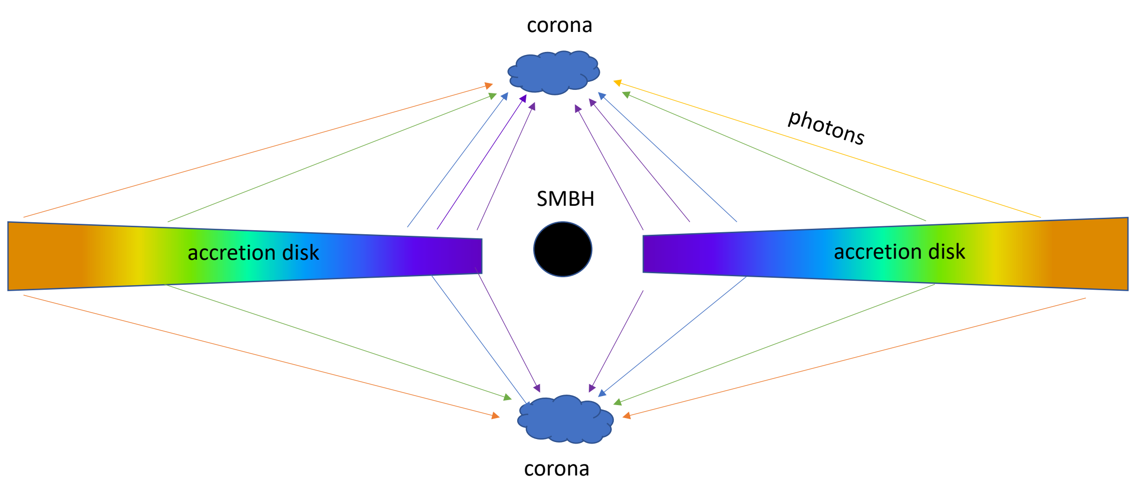

Figure 2.3: Lampposts model of accretion disk corona. Due to the complex magnetic field activity and magnetic reconnections, the plasma would be able to hold above and below the black hole

The electrons in the corona will transfer energy to the photons from the accretion disk because the electrons are ultra-relativistic. The process by which ultra-relativistic

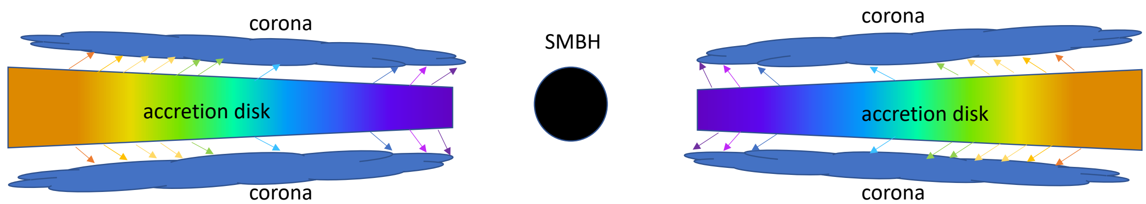

Figure 2.4: Sandwich model of accretion disk corona. The plasma are hovers over the accretion disk directly, sandwiching the accretion disk in between.

electrons give energy to the photon is known as Inverse-Compton scattering. When high energy photons gives energy to electrons the process is called Compton scattering. In this case the energy lost by the electron to the photon is proportional to $1/(1-\frac{v^2}{c^2})$, and so this is the same amount of energy gained by the photons. This implies that the more energy the electrons have, the more energy they give to the photons. [33].

From the Inverse Compton Scattering process, the corona scatters off X-ray photons in all directions, and some of them will be reflected by the accretion disk (Fig 2.7).

The X-rays reflected by the accretion disk have two intrinsic features: the fluorescence line (iron emitting a photon due to the absorption of X-rays), and the Compton hump [1], both of those features will be discussed in the Spectroscopy section.

X-ray spectroscopy

When the photons have been emitted by the accretion disk, some will reach the corona and be Inverse-Compton scattered. The photons received by the corona are uniformly scattered. Thus, the disk spectrum will be stretched to the X-ray energy range by this process (show Fig 2.6).

From this process we obtain a spectrum that is described by a power-law, which

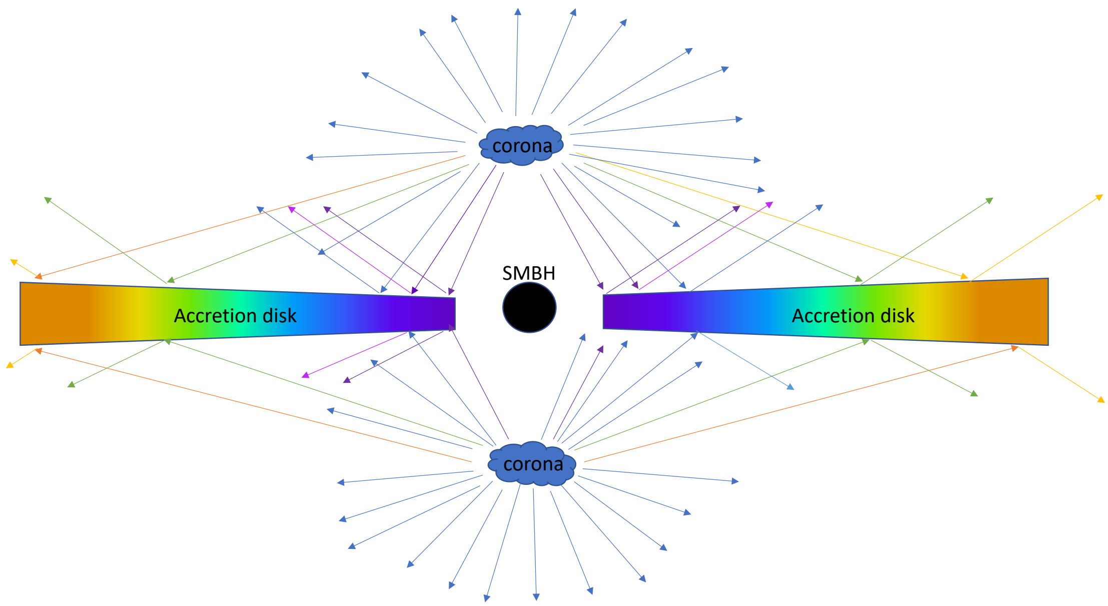

Figure 2.5: The heated X-ray photons, from the corona emits in all directions. Some of those photons have been reflected by the accretion disk and those reflected photons have unique signatures of fluorescence spectrum and Compton Hump ([21])

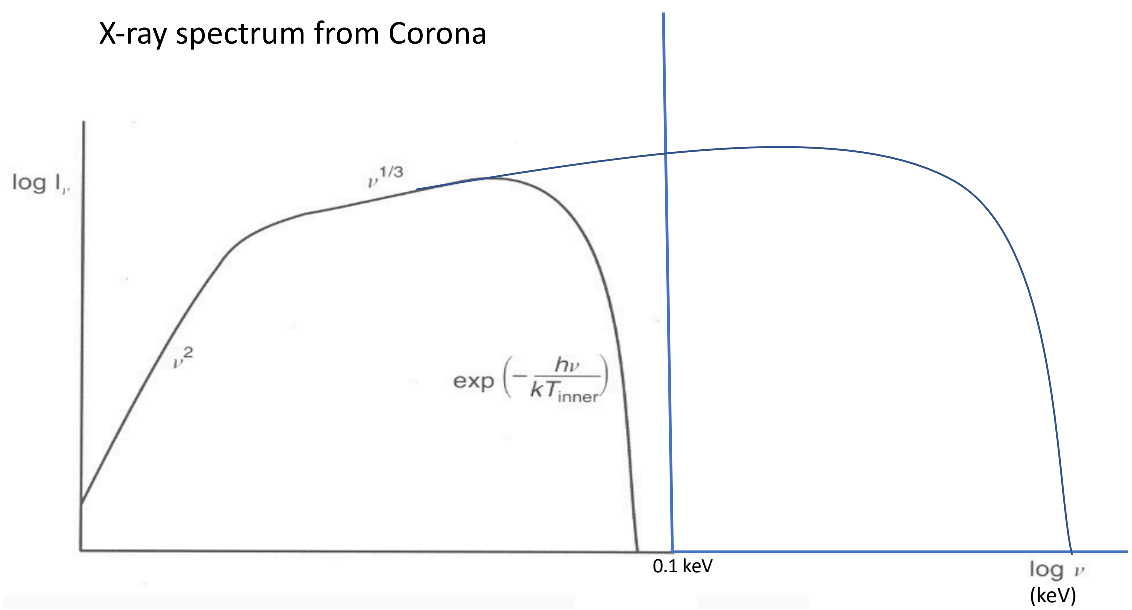

Figure 2.6: All photons are uniformly up-scattered (photon scattered to higher energy) by the ultra-relativistic electrons)

is the flat part of the spectrum, when ploted on the log-log scale. The plot shows an exponential cut off at a higher energy levels.

The exponential cut off is due to the relativistic electrons having a finite energy distribution and the disk spectrum also being finite. As the electron energy becomes greater the cross section for the electron and photon to interact decreases. Therefore, when a photon interacts with the electron, the photon will gain some energy from the electron. But it is the electrons temperature that determines the amount of energy allowed to be transfer to photons. The electrons can't transfer more energy than it has to the photons. The exponential cut off tells us the physical temperature of the electrons in the plasma.

<u>Power-Law</u>

The power law component models the distribution of photon energies scattered by the corona. The X-rays produced by the Inverse-Compton are nonthermal, meaning we can't reproduce the spectrum by adding a series of black-body models together. But the spectrum is well represented by the power law. A detailed derivation is not exactly trivial, they are presented in the Radiative Processes in Astrophysics by Rybicki and Lightman (pg. 202- 213) [30]. From the derivation we can find the number of photon per cm^{-2} per second is proportional to n(E)= $n_0 E^{-\Gamma}$). The power law component is described by the photon index Γ. Since we know how the photon index relates to the energy index, we can determine the photon index and then determine the energy flux power law. We obtained data in the from of the number of photons per cm^{-2} per second. The photon flux is represented with n(E), and E n(E) would be the energy flux. If we plot the photon flux respect to its energy in the logarithmic scale we obtain:

$$\mathrm{n(E)dE} = \mathrm{n(E)E}\frac{\mathrm{dE}}{\mathrm{E}} = \mathrm{En(E)d(log(E))} = \mathrm{f(E)d(log(E))} \tag{2.1}$$

$$f(E) = n_0 E^{-\alpha} \tag{2.2}$$

In this case $\alpha = \Gamma - 1$, α is known as the energy index, but frequently we work with photon index directly. When we present the spectrum this way, we obtain a flat line for $\Gamma = 2$, and if it is less than 2 the power law is increasing with energy, when it is greater than 2 then it is decreasing with.

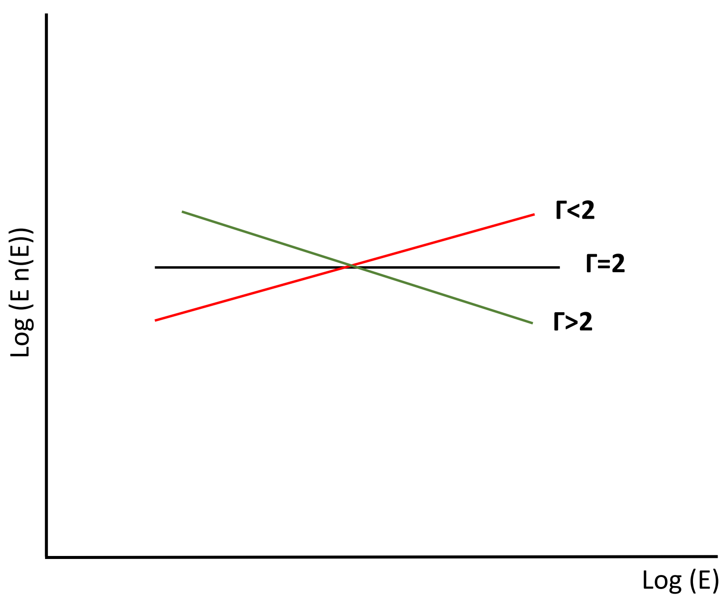

Figure 2.7: Power law illustration with different values of Γ

When the power law is steep towards the high energy, it suggests that the photons are possibly scattered many times before escaping from the corona. It is believe that the power law's shape indicates the mean free path of the photon before they escape from the corona. Thus, we can possibly infer the corona density from the geometry.

Although the power law and the high energy cut off are the main features of the X-ray spectrum, the X-ray spectrum does have other features in addition to these two components. We also see emission lines and a hump present. The strongest emission line that is contributed to by the iron absorbing of an X-ray and re-emitting it at an specific energy is known as the fluorescence line. And the hump comes from X-rays reflecting off the accretion disk and is known as the Compton Hump.

Fluorescence line and Compton Hump

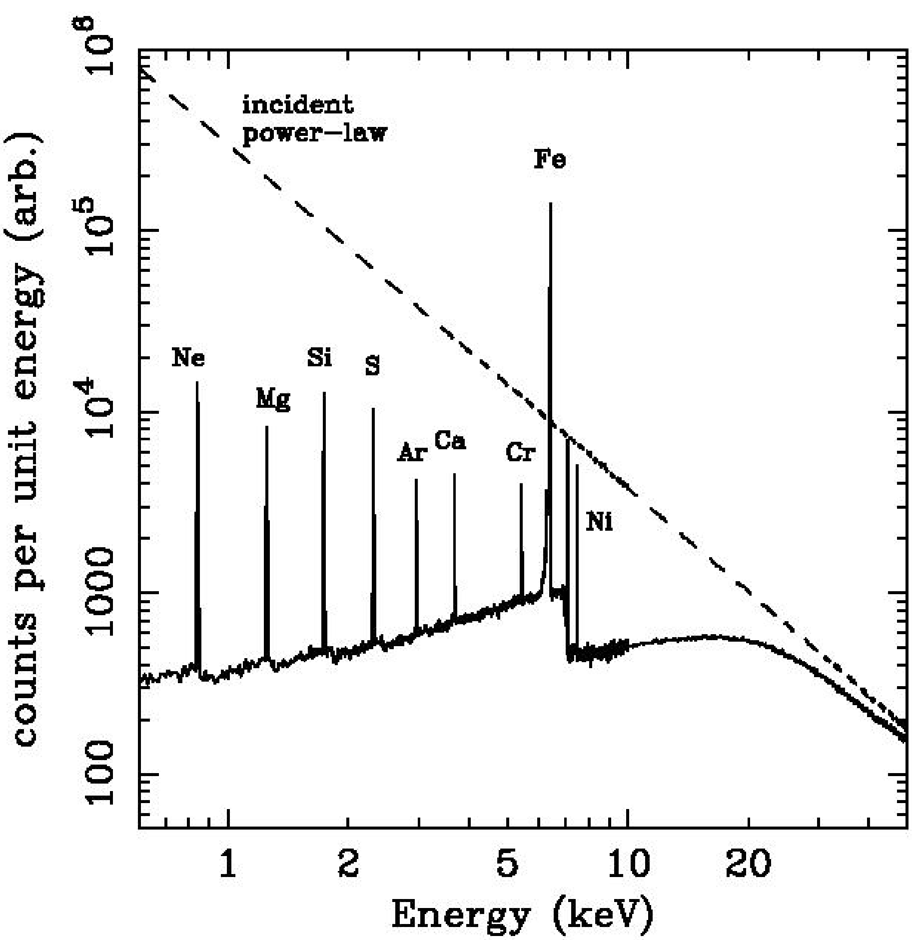

Figure 2.8: Spectrum generated by Monte Carlo Method, shows a strong K_α emission line at 6.4 keV follow by a Compton Hump (Plot credit: [1])

We know that the accretion disk is at a much cooler temperature than the X-rays from the corona (Recall from Fig 2.1). The iron atoms are not likely to be completely ionized. The K-shell electrons then can then either absorb the X-ray and re-emit it at an particular energy of 6.4 keV, or it can eject out an electron with the energy it absorbed (known as Auger effect). The emission line we observed in the X-ray spectrum at 6.4 keV is the fluorescence line. [13]. Following the fluorescence emission line is the Compton Hump. It is believed that the hump is produced by the combination of scattering and absorption by “cold” matter ($T < 10^6$K) [37]. I wish to point out that although both the fluorescence line and the Compton hump are an indication of X-ray reflection, these analyses conducted constrain the strength of the Compton hump. It intimately depends on the geometry, observed orientation, absorption, position of the corona, and the location of the reflection of the X-ray among other factors. that makes this parameter entangled with all of the parameters we are analyzing (power-law, high energy cut off, and fluorescence line). But from the theoretical prediction the Compton hump should be maximized with a peak around 20-30 keV [20].

Time Variability

Another important character which is not directly imprinted on the energy spectrum is the time variability. As mentioned in the introduction, the SMBH with accretion model explains the short time flux variation of AGN. It is believe that the time variability is caused by the physical or dynamical variation of the AGN system. It could have been caused by the resizing of the broad line cloud (thus changing in the absorption parameter) or by the change in outflow in the accretion disk, or the alternation of jet internal structure, but the study has shown that the high energy photons (e.g. Gamma-rays) could double its flux in as short as a couple of hours, and the optical band could vary within minutes [36]. Recent study has expanded the time variation into the X-ray range [44]. The time variability analysis between higher and lower X-ray energy band gives information about the geometry of the media which scattered the photons.

METHODS OF ANALYSIS

Upon knowing the structure and physical meaning of each part of the spectrum we are ready to fit and analyze the spectrum. The goal is to fit the data collected by the observatory, and determine the value of each parameter. Then each of the parameters gives information about the system we observed. The tool we employed to conduct the fitting of the spectrum data is XSPEC [27]. It is a command driven interface X-ray spectrum fitting tool developed by HEASARC Astrophysics Science Division at NASA Goddard Flight Center.

Xspec is designed to work with all X-ray spectrometers. It is able to be accessed through Linux, and has a separate interface built in python called PyXspec [27]. We have conducted a rough approximation from the Xspec, and then a detailed reproducible analysis via python script.

For the rest of the chapter I will focus on the discussion of the method and procedure we have employed to conduct the analysis on the data we obtained. We implemented this in the Mrk 110 section, see section in Mrk 110.

Background subtraction

First, we need to subtract the noise from the data. The source count rates will most likely been influenced by the background counts contributed by the background stars, cosmic rays, etc. To get the true source count, we must subtract this influence. To use this method we selected an area that does not contain the source (Fig 3.1 shown as green circle), then count contributions from the background, and divide by the total area within the circle (that will give us an density of back ground counts per unit area). Similarly, we took an area of the source count (Fig 3.1 shown in the red circle), then use the background count density multiplied by the source area to get the total background count contribution to the source area. Finally we subtracted the raw source data with the background count contributed to the source area to get a background free set of data.

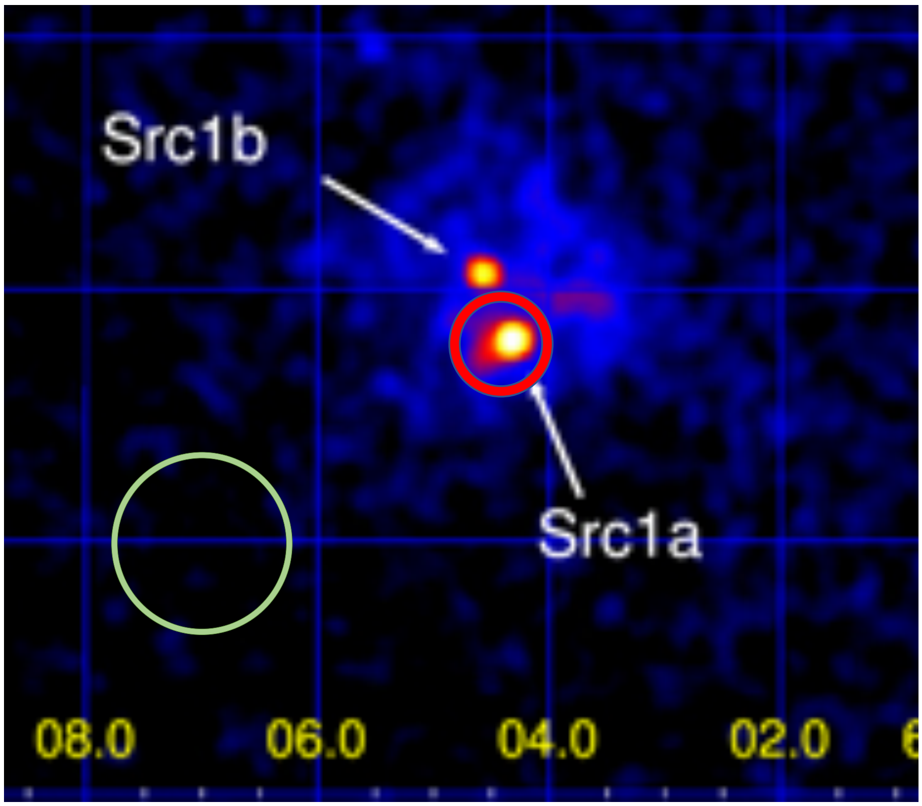

Figure 3.1: Example X-ray detection from NuSTAR observation to Supernova Remnant-molecular Cloud (IC 443) (Plot credit: [17])

Data Binning

Once we obtained the processed data from background subtraction. We can plot the data with count flux with respect to energy on a log-log scale, as shown in the raw data (Fig 1.11). However not all of the data is useful due to too many photons (saturation) the exposure time for our data is 1.778×10^5sec, and in average we have

1 photon per second. Therefore, we have 10^5 counts, the data is shown in Fig 3.2 and are contribute from FPM-A (black) and FPM-B (red).

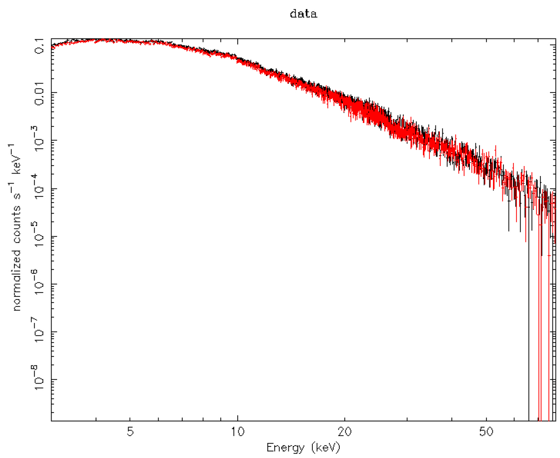

Figure 3.2: Log-log plot of NuSTAR data from FPM A B. The data range shown in the plot is from 3.0-79.0 keV as this is the NuSTAR detector energy range [28]

Data from the higher energy band has a greater error in counting because we don't have quite as many photon counts at the higher energy band, but in the lower energy range, we have an excessive amount of photon counts (e.g. $E < 10$keV). In order to improve the fitting to the data, we want to capture the major features of the spectra curve, but not over saturate it with the detailed fluctuations in the photon counts.

For example if we bin the data 20 values into 1 bin (as shown in Fig 3.3) we see the spectrum trend and its features are better, and the error contributed from the higher energy range shows less influence on the data.

The binning doesn't change the data fundamentally, so the fitting will not be influence by the binning of the data (as long as the data is not binnning too much, otherwise the feature of the data will be smoothed out by over averaging values).

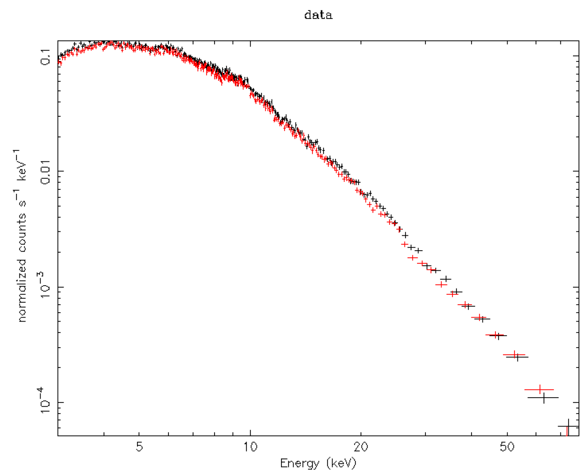

Figure 3.3: Data after binning every 20 values together into one value

Modeling and Statistics

The way we can quantify how accurate the fitting is, an be done through the Chi-square test. The goal is to build a model which fits the data to produce a reduced chi-square as close to 1.0 as possible.

The Chi-square is defined by:

$$\chi^2 = \sum_{i=1}^{n} \frac{(S_i - M_i)^2}{\sigma_i^2} \qquad , \tag{3.1}$$

Hence, S_i is the amount of counts in i^{th} bin of the data, n is the number of data bins, M_i is the fitted number of counts for the i^{th} bin, and σ_i is the expected error from the fitting. The residual of the fit is the difference between the data value and the fitted values. The reduced chi-square value is $\frac{\chi^2}{m-n}$. Here, m is the total number of data points, and n is the amount of parameters we used to construct the model to fit the data.

Using the model we build, we can either multiply the components together, or adding the components depending on the physical processes presented in the data. Xspec has many built in physical components that we can use to construct best fit to the spectrum. For example, the ”tbabs” or ”phabs” component represent the absorption parameter of the hydrogen column density. In the case of Mrk 110 observations we know the hydrogen column density is 1.33×10^{20} atoms per cm^2 [6]. An example of a simple model is “$modelphabs * (powerlaw)$” which means we are modeling the spectrum with a power-law but offset by the amount of absorption along the observing direction. The data showed in Fig 3.4 is an example of fitting done by this model; the chi-square statistics gives 1872.85/1605. When we look into the residual from this fit,the residual around 6.4 keV is significant.

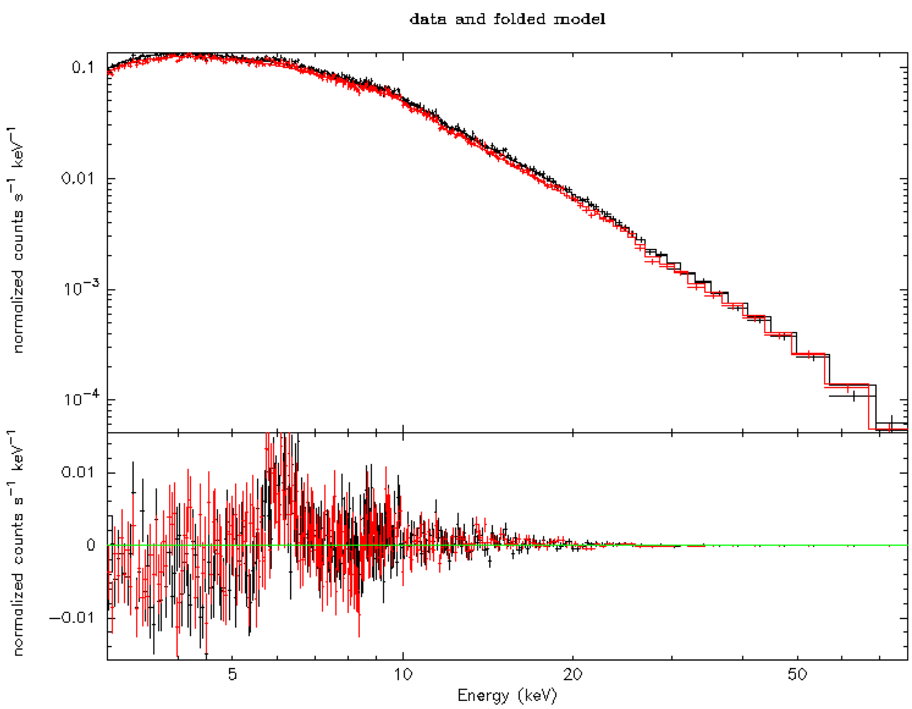

Figure 3.4: Model fitted with a simple power-law and a absorption nH $= 1.33 \times 10^{20}$atom/cm^2

The fit suggests the simple model doesn’t capture all the physical components such as the fluorescence line from the spectrum. In order to improve the fit, we add an component of red-shifted Gaussian to fit the emission line. As Shown Fig 3.5 the reduced chi-square gives $\frac{1724.51}{1599}$, therefore the test is significantly improved. The way we determine if the chi-square test is significantly improved, is to check if chi-square improved by at least 1 sigma (corresponding to a value of 2.7).

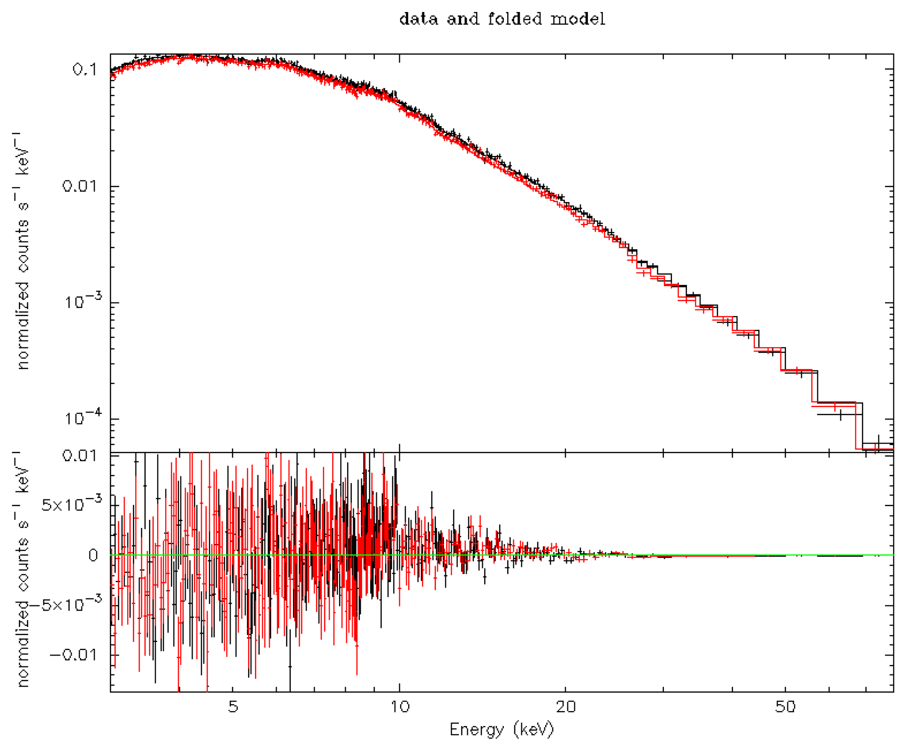

Figure 3.5: Model with power law and red shifted Gaussian. The Gaussian captures the fluoresces line.

When we look at the residual there is quite bit of contribution from the higher energy spectrum (e.g. 8-20 keV). Since the large residual was contributed from the higher energy band, the only physical process we haven't considered at the higher energy data is the cut off energy. So if we then replace the power-law by a cut off power law (shown Fig 4.5) as expected the residual improves at higher energy spectrum. This procedure has a reduced chi-square of $\frac{1613.52}{1597}$. The chi-square result has improved by about 96 sigma.

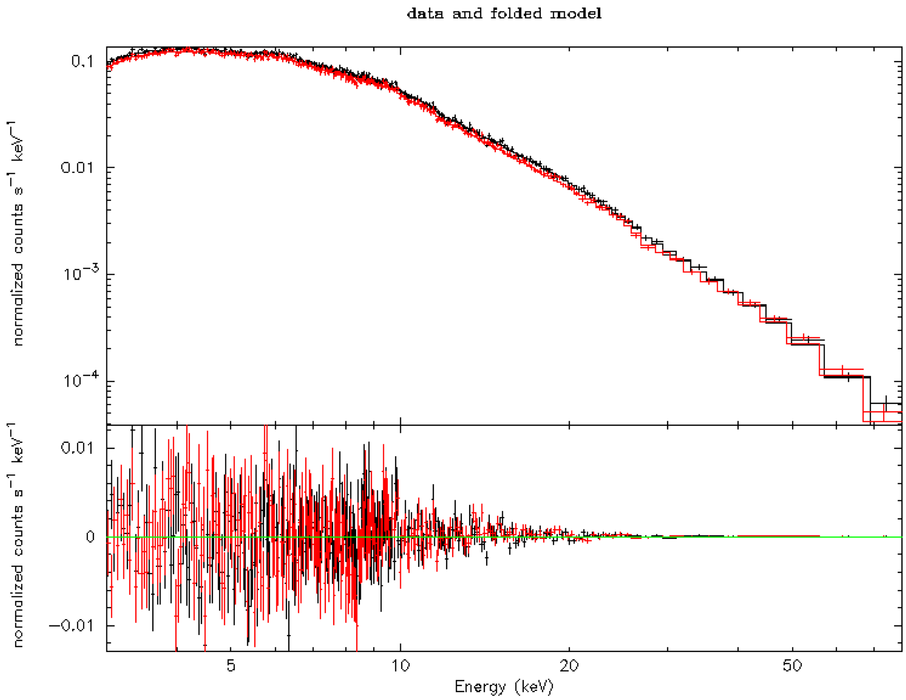

Figure 3.6: Model considered a cut-off power law and red-shift Gaussian capturing the fluorescence line. This model gives the best chi-square value.

MRK 110

Now we are ready to talk about Mrk 110 (also Mrn 110). Its full name is Markarian 110. Markarian is a classification of galaxies which has an excessive amount of UV emission, with a blue core normally. Mrk 110 is a source which seems to “violate” the fundamental plane ofn an accreting black hole. And our goal is to understand the odd radio signal behavior through study the X-ray emission. Following, I present the report on the analysis we’ve conducted on the NuSTAR data for Mrk 110.

Introduction

The co-evolution of the supermassive black holes (SMBHs) and their host galaxies has been one of the most interesting mysteries astrophysicists have been trying to understand. After decades of study, astronomers were able to determine that the SMBHs influence the host galaxy by inducing relativistic outflows from accretion [23]. Despite relativistic jets being one of the most powerful feedback mechanisms [4], the details of the jet formation remain a mystery. If we are able to determine the cause and formation of the relativistic jets, it would be helpful for us to be able to quantify the power of feedback from this mechanism. From the fundamental plane of black hole activity, we would expect the same radio luminosity produced by black holes with the same accretion rate and mass ([35] [29]). However, this is clearly not true as previous observations of galaxies such as Mrk 110 and 3C 120 show. Both sources have the same black hole mass and accretion rate, but galaxy 3C 120 has a very different radio luminosity compared to Mrk 110 [9]. This leads to a pressing question: what are the X-ray features which determine the efficiency of jet production for a high Eddington accreting AGN?

Seyfert 1 galaxies are one of the frequently studied AGN. Their optical emission is dominated by nuclear continuum emission, narrow and occasionally broad emission lines. They also display strong nuclear X-ray emission and sometimes a weak small-scale radio jet. We are particularly interested in the Seyfert 1 galaxy Mrk 110 due to its suppressed radio luminosity. It accretes at a high Eddington ratio, with virial factor f= 8-16, which is high compared to most of the Seyfert galaxies with an average of $< f >= 1$ [31], Studies from 2007 have shown that there is a correlation between the accretion rate at the Bondi radius and kinetic luminosity of the jets [34].

The source we study in this paper — Mrk 110— has a black hole mass of $\mathrm{Log(M_{BH})} = 7.32 \pm 0.12\ M_{\odot}$, and X-ray luminosity of $L_X = 9.0 \times 10^{43}$erg/s [19], redshift of 0.0353, black hole inclination of 21 ± 5 degrees [47], and accretion disk inclination of 60 degs [16]. There are previous studies conducted on Mrk 110 by [24] & [16]. Hiroshi's team analyzed observations from Suzaku; they found the to be $1.84{\pm}0.02$, the fluorescence line at $6.38{\pm}0.03$ keV, a reflection component of $2.7{\pm}0.6$, and a high energy cut off at 35^{+10}_{-6} keV. The power law component is anti-correlated with the black hole mass and correlated with the accretion rate [25]. The fluorescence line (at 6.4 keV) probes the inner region of the black hole [32], and the Compton hump probes the thickness of the disk [40]. Therefore, it is crucial to determine the parameters which govern the power law component, ionized and neutral reflection, as well as the high-energy cutoff. Those parameters provide an important clue about the AGN physical environment, and an answer to the behavior of the suppressed flux. In Monica's team they found the power law of $1.3^{+0.2}_{-0.1}$ for hard X-rays, and $2.5^{+0.3}_{-0.1}$ for soft X-rays, and a 0 width fluorescence line from XMM observations. However, in our analysis we found slightly different results.

We report the results from the 2017 NuSTAR observation of Mrk110, comparing our spectral analysis results with the existing studies of those component with the

SWIFT and XMM observations [39] [16]. Here, we find the power-law components in good agreement with the previous studies (results shown in Table 1). However, we detect changes in the iron line and reflection component compared to previous studies from Suzaku and XMM observations.

Interestingly, we detect a strong fluorescence signal, but a hardening cut off energy, suggest a very small reflection component. We are expecting the reflection component and the iron line signal to coexist with each other [1], but from NuSTAR data we only observed the iron line and not the reflection component. The details of the possible causes of these phenomena are mentioned in the discussion section.

In this paper, we will first report on processing of the data (Section 4), follow by the variability and spectra analysis (Section 4), and finally in the discussion we will address how the results we found compare to XMM and SWIFT observation, and intriguing hardening of X-rays along with the fluorescence line signal.

Table 1.

Observatory	ID	Exp. Time	reported Γ
XMM-Newton	02011305010	48 ks	1.75 ±0.1(2006) 1.40 ±0.1(2007) 1.34 ±0.1(2018)
Suzaku	702124010	80 ks	1.84 ±0.02(2018)
NuSTAR	60201025002	184 ks	1.74 ±0.01(2019)

The existing Mrk 110 photon-index from XMM, SWIFT and NuSTAR observations. The NuSTAR observation report here comes from our best fit.

Observations

In this paper we analyzed the $\sim 185\,\mathrm{ks}$ *NuSTAR* observation of Mrk 110 taken in January 2017 (ObsID 60201025002). Our data reduction starts with producing cleaned up event files using the nupipeline tool. Our SAA screening criteria for this purpose is based on the *NuSTAR* SAA Filtering Report for this observation, chosen to optimize the background level and exposure time. From the cleaned event files, we extract spectra and light curves using nuproducts. The source and background regions are selected to be both circular with a radius of 65" and 100", respectively. We produced light curves in four energy bands: 3-5 keV, 5-10 keV, 10-20 keV and 20-30 keV each with time resolution of 1.5 ks.

Analysis Results

Variability Analysis

We begin our analysis with investigating whether there are flux changes in the Mrk 110. We employed years of variability data from Rossi X-ray Timing Explorer (RXTE [45]) and Neil Gehrels Swift Observatory (SWIFT [39]). The detection energy range for RXTE is 2-10 keV and SWIFT is 0.2-10 keV. The RXTE data is binned to 15 days, and the SWIFT data are binned to 29 days. Figure 1 shows the light curves of the two bands. From both RXTE and SWIFT we conclude that Mrk110 does have a flux changes by a factor of 2 on the long timescales. Unfortunately, RXTE had been terminated during the NuSTAR observation operation period, but when we compare SWIFT data with available RXTE data, the variations in the light curve shows they are correlated. We can see there is a small increase of flux in detected during NuSTAR observation.

Next, we conduct a time variation analysis on NuSTAR lightcurves to understand if there are any short-timescale variations. The analysis results shown in Figure 2 are fit with a constant value to the variation in each energy band, and results suggest most of the variations are contribute by the lower energy bands, where 3-5 keV correspond to $\chi^2/\mathrm{dof} = 407.3/205$, 5-10 keV of $\chi^2/\mathrm{dof} = 397.01/205$. Higher energy band shows

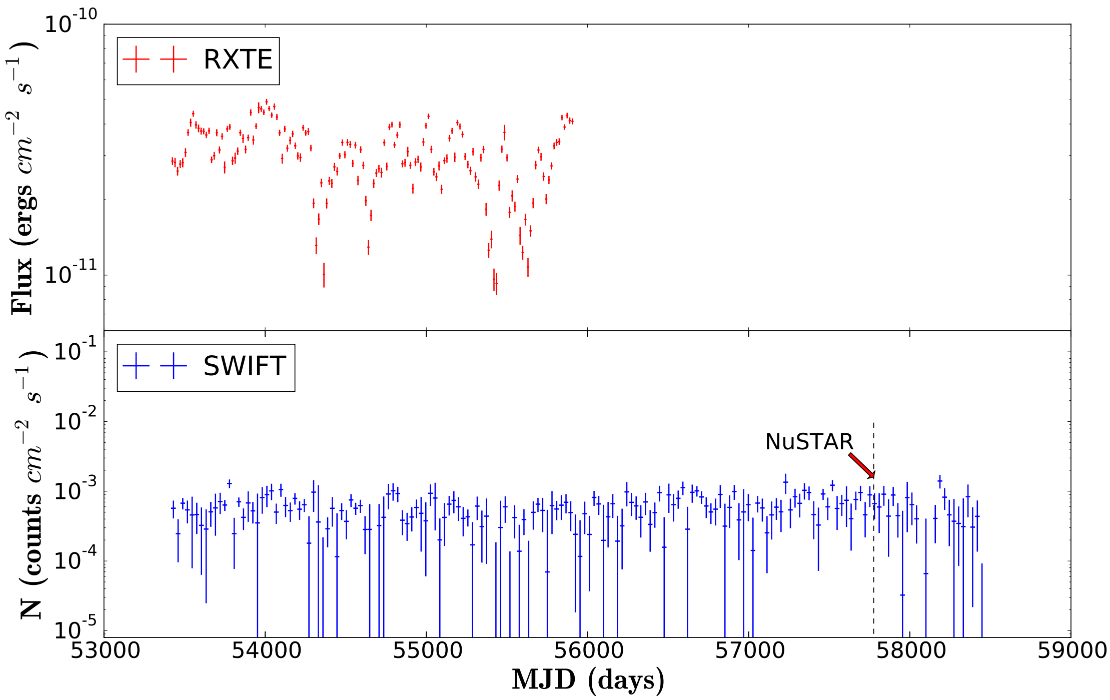

Figure 4.1: Top panel shows the time variation from RXTE during March 2005 to Dec. 2011. The bottom panel shows SWIFT data variation from March 2005 to Nov. 2018. The NuSTAR observation dates are labeled with arrows. RXTE data was binned to 15 days, and SWIFT data was binned to 29 days

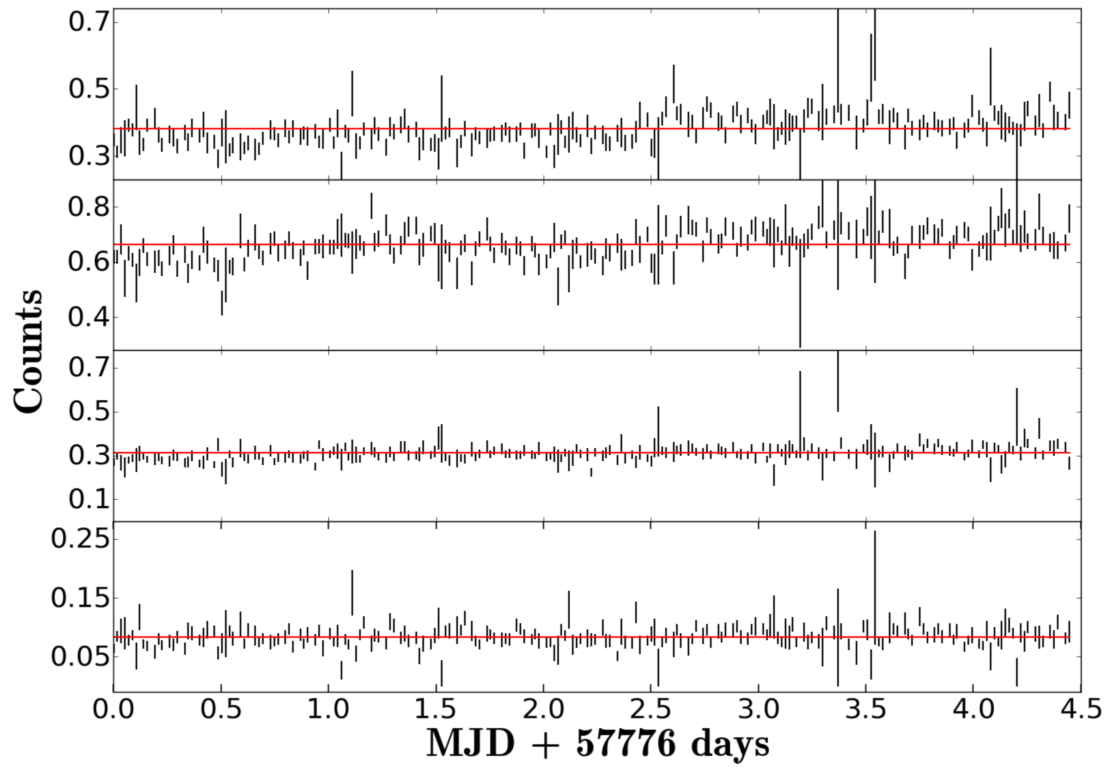

Figure 4.2: Constant fit of four energy bands, red line indicates best fitting constants. The top panel: 3-5 keV with best fit constant of 0.38, second panel: 5-10 keV fitting parameter of 0.66, third panel: 10-20 keV fitted with 0.31, and bottom panel: 20-30 keV fitted with 0.08

minimal variations with $\chi^2/\text{dof} = 263.41/205$ in 10-20 keV, $\chi^2/\text{dof} = 267.55/205$ in 20-30 keV. We wish to understand if the lower energy bands variations were correlated, so we observed the ratio between 5-10 keV to 3-5 keV. Figure 3 shows the variation ratio, and the red line labels the constant difference of 1.7. The chi-square test for the ratio plot has value of $\chi^2/\text{dof} = 247.5/205$. This suggests a strong correlations between variations in those two energy bands. With so little short-term variability, we will follow with an analysis on the average NuSTAR spectra.

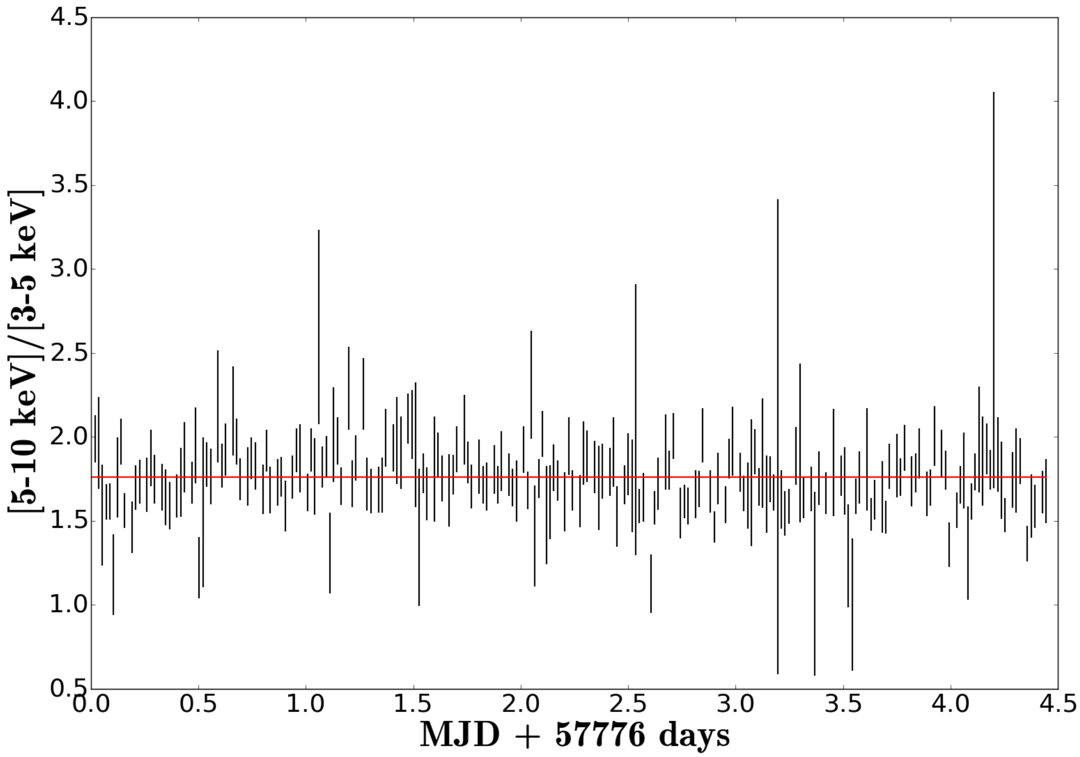

Figure 4.3: Ratio between 5-10 keV band and 3-5 keV band abstract from NuSTAR data. the red line labels 1.7. The chi-square test gives $\chi^2/\text{dof} = 247.52/205$, suggesting a good fit and good correlations between the two energy bands

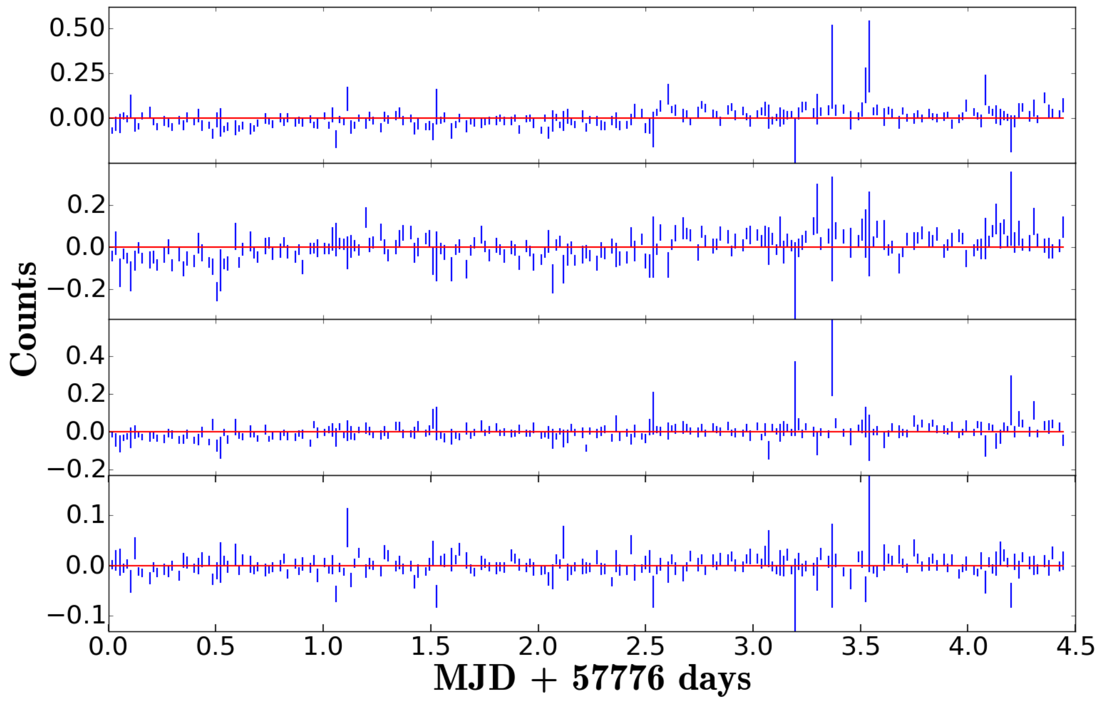

Figure 4.4: Residuals of the four energy bands fitted in Figure 4.2. The reduced chi-square tests are 3-5 keV:χ^2/dof = 407.3/205, 5-10 keV:χ^2/dof = 397.01/205, 10-20 keV:χ^2/dof = 263.41/205, and 20-30 keV:χ^2/dof = 267.55/205. All indicate a good Chi-square fit. The chi-square test is better at higher energy bands, whereas majority we find more variations in the lower energy bands

Spectra Anaylsis

We conducted analysis on Mrk110 with python xspec program Dorman, where the data was taken from NuSTAR observatory on January 23rd,2017 (Obs. ID = 60201025002). The hydrogen column density for Mrk 110 utilize in this analysis is $1.33 \times 10^{20} \text{cm}^{-2}$ nH, with Vern cross-section cross-sect, and Wilms iron abundance F-abund . Wilms model is an absorption model of X-rays in the ISM use for X-ray missions with larger effective areas and increased energy resolution in the energy range ¿ 100 eV). All of the errors are estimated with 90% confidence. We first capture the structure of the spectrum with an absorbed power law (model 1=tbabs*(power)). The photon index found to be $\Gamma = 1.82 \pm 0.02$, with $\chi^2/\text{dof} = 1860.95/1587$ for simple power law model (Figure 4.6 Top).

We see a significant amount of residual contribution from the iron line region, and energy region above 20 keV (shown in Fig 4.5 top). To address the region we first add a red-shifted Gaussian, and fit again with the simple power law. We initialized the width of the Gaussian to be 0 (model 2 = tbabs*(power+zgauss)). This method will tell us whether the Gaussian width is due to detector noise. The result shows the photon index remains the same, and the χ^2 improved significantly, by $\Delta\chi^2 = 106.03$. Despite the fitting being significantly improved, the structure of the residual around the iron line region is not completely eliminated. In order to improve the fit further, we allow the Gaussian to have a finite width (model 3 =tbabs*(power+zgauss)) and the fit has improved residual by $\Delta\chi^2 = 38.79$ with $\Gamma = 1.82 \pm 0.02$ (Figure 4.6 Middle). The iron line width is $(3.34 \pm 0.03) \times 10^{-1}$ keV.

Despite the ratio being reduced in the iron line region, there is a significant amount of residual contributed from the higher energy region(Fig 4.5 middle). Thus, we replace the simple power law to the cut off power law (model 4 = tbabs(cutoffpwl+zgauss)). This model returns $\Gamma = 1.74 \pm 0.02$, $E_c = 130.05 \pm 9.69$

keV and residual improves again by $\Delta\chi^2 = 113.47$. The average spectrum analysis above captures the residual well for an energy region less than 20 keV. However, the ratio plot suggests there are residuals not captured by the models for higher energy region. The energy regions $\geq$ 20 keV are governed by Compton reflection. To reduce the residual in this energy region, we use models which contain a Compton hump to fit the data. We utilized is the neutral Compton reflection model [41], the pexmon model is a model which constructed with a cut off power law, a reflection component, and a self-consistently generated Fe Kα, Fe Kβ, Ni Kα ([21]) for iron line energy region, and a model of Compton shoulder ([1]). The inclination of the disk is assumed to be at 60 degrees ([24]). The reflection component combined with the the self-consistent iron lines and the Compton hump captures the residual at higher energy if it is caused by Compton scattering. Under this model we found $\Gamma = 1.76 \pm 0.02$, and the residual improved compared to the non-cut off power law with Gaussian, $\Delta\chi^2 = 1.05$. Table 1 shows all of the fitting parameters corresponding to the models we used.

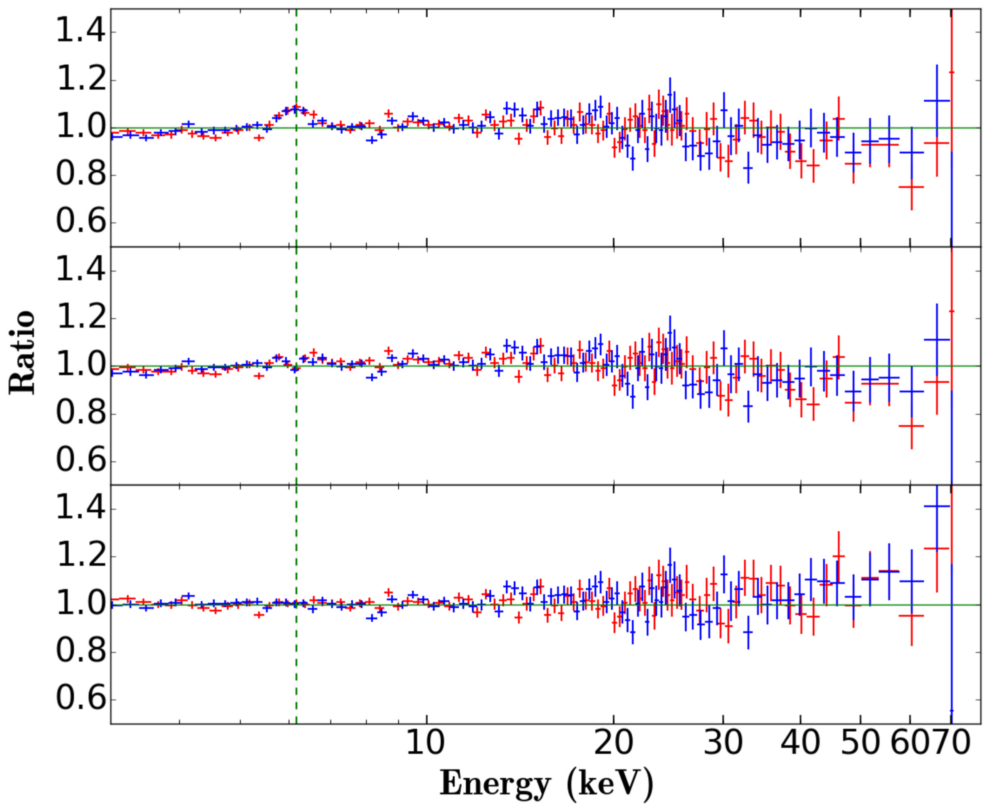

Figure 4.5: Red and blue represent data from NuSTAR FPM-A and FPM-B. The green dash indicates the red-shifted iron line location. The data has been binned to Max=60 and Group=10 for a better plot. Ratio of simple power fit (upper panel), Simple power law with 0 width Gaussian (middle panel),and cut off power-law with finite width Gaussian model (lower panel).

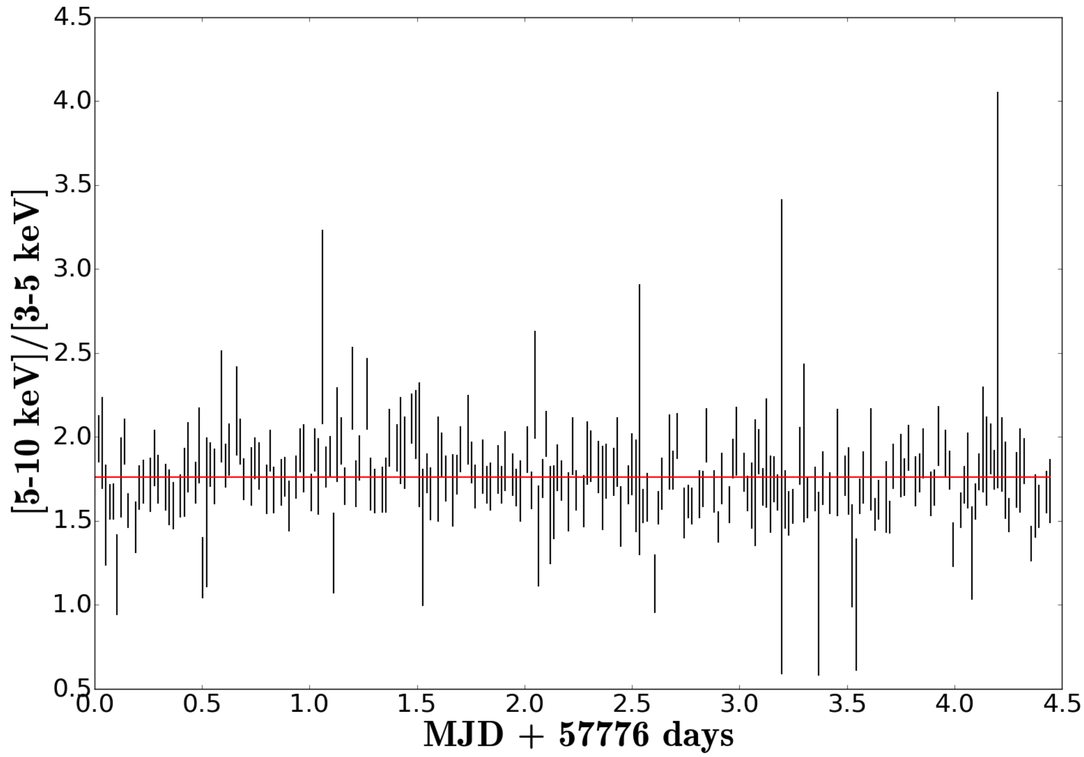

Figure 4.6: Ratio residual for neutral Compton reflection model. Red and blue indicate NuSTAR data from FPM-A and FPM-B. Green dash line indicates red-shifted iron line location. The data has been binned to Max=60 and Group=10 to show the plot better. The ratio is not improved in region > 20 keV.

Table 2. Fitted Parameters with the 6 indicated Models

Model	Parameter	Mrk 110
	nH(cm^{-2})	$0.0133*10^{22}$
	Redshift	0.0353
power law	Γ	1.82 ±0.02
	cal-const	1.11 ±0.01
	χ^2/dof	1860.95/1587
power and zgauss (fix width)	Γ	1.82 ±0.02
	cal-const	$9.22 \pm 0.09 \times 10^{-1}$
	Norm*($cm^{-2}s^{-1}keV^{-1}$)	$(12.5 \pm 0.12) \times 10^{-3}$
	Line Energy(keV)	6.33 ±0.06
	Line Width(keV)	0.0
	Line norm(cm^{-2} $s^{-1}keV^{-1}$)	$(2.21 \pm 0.02) \times 10^{-5}$
	χ^2/dof	1754.92/1585
power and zgauss	Γ	1.82 ±0.02
	cal-const	$9.34 \pm 0.09 \times 10^{-1}$
	Norm*($cm^{-2}s^{-1}keV^{-1}$)	$(12.2 \pm 0.12) \times 10^{-3}$
	Line Energy(keV)	6.39 ±0.06
	Line Width(keV)	$(33.4 \pm 0.29) \times 10^{-2}$
	Line norm($cm^{-2}s^{-1}keV^{-1}$)	$(3.84 \pm 0.04) \times 10^{-5}$
	χ^2/dof	1715.87/1584
cutoff power law with zgauss	Γ	1.74 ±0.02
	cal-const	$(9.42 \pm 0.09) \times 10^{-1}$
	E_c (keV)	130.05 ± 9.69
	Norm*($cm^{-2}s^{-1}keV^{-1}$)	$(11.1 \pm 0.1) \times 10^{-3}$
	Line Energy(keV)	6.37 ±0.06
	Line Width(keV)	$(29.2 \pm 0.29) \times 10^{-2}$
	Line norm ($cm^{-2}s^{-1}keV^{-1}$)	$(3.31 \pm 0.03) \times 10^{-5}$
	χ^2/dof	1602.48/1582
pexmon model	Γ	1.78 ±0.02
	Cal-const	1.18 ±0.01
	E_c (KeV)	104.03 ± 5.5
	Norm*($cm^{-2}s^{-1}keV^{-1}$)	$(17.76 \pm 0.93) \times 10^{-3}$
	R	$(2.02 \pm 0.02) \times 10^{-1}$
	χ^2/dof	1663.91/1583
pexrav and zguass	Γ	1.75 ±0.02
	Cal-const	1.30 ±0.01
	E_c (KeV)	129.03 ± 8.26
	Norm*($cm^{-2}s^{-1}keV^{-1}$)	$(7.95 \pm 0.93) \times 10^{-3}$
	R	< 0.02
	χ^2/dof	1602.07/1580

Calibration constant in power fit is 2nd detector data respect to 1st detector data. 1st data calibration is fix to be 1. All models are multiplied by nH and calibration constant.

Figure 4.7: fitted parameters

CONCLUSION

From the study of the timing variation comparing RXTE and SWIFT light curves, we found that the X-ray flux changed by a factor of 2 for Mrk 110. The NuSTAR light curve shows an amplification of 1.7 between lower (3-5 keV) and higher (5-10 keV) energy bands. The power-law component of Mrk 110 is well agreed with the observation from Suzaku study which has value of 1.84 ± 0.02, but is slightly higher than the XMM data which was 1.34 ± 0.1. We find a nearly zero reflection component with < 0.02, which disagrees with the previous study of the Suzaku report of a reflection value of 2.7 ± 0.6 [24] and XMM of 8.14 ± 0.12 [14]. We find a large cut off energy of 130 ± 9.69 keV, where the Suzaku analysis suggests a much lower value of 35^{+10}_{-6} keV. Also, we report a larger Iron line width of $0.30^{+0.03}_{-0.04}$ keV, compared to a line width of < 0.08 keV from Suzaku, and 52^{70}_{36} eV from XMM [7]. Despite us have a strong signal for the fluorescence line at 6.37 ± 0.06 keV, we hardly see any reflection component from the data. This is an intriguing result, since the fluorescence iron line is produced by reflecting X-rays on the accretion disk and ionizing irons in the disk [32]. Therefore a strong iron line should be accompanied by a strong reflection component. If there is no X-ray reflection from the disk, then we must find other explanations for how the fluorescence iron line has been produced.

We suspect the extreme low reflection component is due to jet production. It is possible that the hardening of the cut off energy is due to the jets beaming, since recent studies from NuSTAR observations on 3C 273 and Mrk 421 which show similar results for the hardening effects of X-ray spectrum [15]. The higher energy photons are contributed by Compton scattering the synchrotron photons, which are most likely produced by the jets. However, the true nature of the cause for this phenomenon still requires a further investigations.

REFERENCES CITED

[1] Compton reflection and iron fluorescence in agn and gbhcs. *Invited review at the workshop on "High Energy Processes in Accreting Black Holes"*, page 15, 10 1998.

[2] J. V. P. J. A.M.Bleeker. X-ray spectroscopy in astrophysics. *EADN School X Amsterdam, The Netherlands 1997*, pages 320–321, Sept. - Oct. 1997.

[3] J. Antonucci, R.R.J.; Miller. spectroopolarimetry and the nature of ngc 1068. *Astrophysical Journal*, 297:621–632, 10 1985.

[4] M. U. A.Y. Wagner, G.V. Bicknell. Driving outflows with relativistic jets and the dependence of agn feedback efficiency on ism in-homogeneity. *Astrophysical Journal*, August 2012.

[5] V. Beckmann and C. Shrader. Active galactic nuclei. 28:2, 2012.

[6] V. Beckmann and C. Shrader. Active galactic nuclei. 28:95, 2012.

[7] I. K. W. Boller, Th. ; Balestra. Xmm-newton observation mrk 110. *Astronomy Astrophysics Journal*, 465:87, dec 2007.

[8] Caltech. NuSTAR Bringing the High Energy Universe into Focus. `https://www.nustar.caltech.edu/page/about`, 2012. [Online; accessed 18-April-2019].

[9] A. P. J. S. G. e. a. Chatterjee, Ritaban; Marscher. Disk-jet connection in the radio galaxy 3c 120. *The Astrophysical Joournal*, 704:1689–1703, 10 2009.

[10] E. Costa and R. e. a. Bellazzini. Polarix: a pathfinder mission of x-ray polarimetry. *Experimental Astronomy*, 28:137, 05 2011.

[11] e. a. Di Matteo. Energy input from quasars regulates the growth and activity of black holes and their host galaxies. *Nature*, 433:604–607, Feb. 2005.

[12] P. N. Dr. Jim Lochner, Meredith Gibb. Xray focus.gif. *Images produced by NASA*, pages 7P–12P, July 2008.

[13] A. F. M. R. L. S. et al. X-ray fluorescence from the inner disc in cygnus x-1. *Monthly Notices of the Royal Astronomical Society*, 238:729–736, 05 1989.

[14] G. D. R. G. S. D. et. al. Discovery of hard x-ray delays in the x-ray emission of the seyfert 1 galaxy markarian 110: Possible evidence of comptonization. *The Astrophysical Journal*, 651:L13–L16, Oct 2006.

[15] J. A. D. M. A. D. R. B. et. al. The nustar extragalactic survey: First direct measurements of the gsim10 kev x-ray luminosity function for active galactic nuclei at z ¿ 0.1. *The Astrophysical Journal*, 815:66, Dec. 2015.

[16] M. V. C. M. S.-L. G. F. H. et al. A comprehensive approach to analyzing the xmm-newton data of seyfert 1 galaxies. *Astronomy Astrophysics Journal*, 530:A125, May 2011.

[17] S. Z. X. T. X. Z. et al. Nustar detection of a hard x-ray source in the supernova remnant - molecular cloud interaction site of ic 443. *High Energy Astrophysical Phenomena*, 125, 05 2018.

[18] E. K. J. S. A. F. etc al. High energy astrophysics phenomena. 01 2019.

[19] E. G. B. P. M. R. Fender. Assessing luminosity correlations via cluster analysis: evidence for dual tracks in the radio/x-ray domain of black hole x-ray binaries. *Monthly Notices of the Royal Astronomical Society*, 423:590–599, May 2012.

[20] I. George and A. Fabian. X-ray reflection from cold matter in active galactic nuclei and x-ray binaries. *Monthly Notices of the Royal Astronomical Society*, 249:352–367, 11 1990.

[21] I. George and A. Fabian. X-ray reflection from cold matter in active galactic nuclei and x-ray binaries. *Monthly Notices of the Royal Astronomical Society*, 249:352–367, March 1991.

[22] M. Hawkins. Timescale of variation and the size of the accretion disc in active galactic nuclei. *Astronomy and Astrophysics*, 462:581–589, 11 2006.

[23] T. M. Heckman and P. N. Best. The coevolution of galaxies and supermassive black holes: Insights from surveys of the contemporary universe. *Annual Review of Astronomy and Astrophysics*, 52:589–660, August 2014.

[24] S. T. H. e. a. Idogaki, H Hiroshi; Ohmura. Study of nature of corona in narrow line seyfert 1 galaxies. *Public Astronomy Society, Japan (2014)*, pages 1–13, May 2018.

[25] T.-L. Ishibashi, W.; Courvoisier. X-ray power law spectra in active galactic nuclei. *Astronomy and AStrophysics*, 512:id.A58, March 2010.

[26] R. Kalia. Accretion disk. `http://www.reneekalia.com/accretion-discs/`, 2017. [Online; accessed 19-April-2019].

[27] C. G. Keith Arnaud and B. Dorman. An x-ray spectral fitting package. *HEASARC, Astrophysics Science Division*, pages 1–4, 10 2018.

[28] T. Kitaguchia. Nustar observatory guide. *NuSTAR Guest Observer Program*, page 4, August 2014.

[29] H. F. E. Krding and S. Markoff. Jet-dominated accretion flows and the radio/x-ray correlation. *American Astronomical Society*, 414:895–903, Feb 2004.

[30] G. B. B. . A. P. Lightman. Radiative processes in astrophysics. pages 202–213, 2004.

[31] H. B. J. Liu, H.T.; Feng. A new method to measure the virial factors in the reverberation mapping of active galactic nuclei. *Monthly Notices of the Royal Astronomical Society*, 466:3323–3330, April 2017.

[32] M. Longair. High energy astrophysics. 1st edition. *Cambridge University Press*, page 645, 2011.

[33] M. S. Longair. High energy astrophysics. 28:539, 2011.

[34] S. Merloni, Andrea; Heinz. Measuring the kinetic power of active galactic nuclei in the radio mode. *Monthly Notices of the Royal Astronomical Society*, 381:589–601, Oct. 2007.

[35] S. D. M. T. Merloni, Andrea; Heinz. A fundamental plane of black hole activity. *Monthly Notices of the Royal Astronomical Society*, 345:1057–1076, November 2003.

[36] M. C. J. N. H. Miller. Microvariability in seyfert galaxies. *The Astronomical journal*, 125:1811–1816, 04 2003.

[37] T. L. Miller. X-ray absorption and reflection in active galactic nuclei. *High Energy Astrophysical Phenomena*, 238, 03 2009.

[38] NASA. NuSTAR Educator's Guide. `http://www.NuSTAR.caltech.edu/`, 2017. [Online; accessed 19-April-2019].

[39] NASA. Mrk 110 data. `https://swift.gsfc.nasa.gov/results/transients/weak/Mrk110/`, Dec. 07, 2018. [Online;].

[40] M. G. G. M. M. R. Changing look: from compton-thick to compton-thin, or the rebirth of fossil active galactic nuclei. *Monthly Notice of the Royal Astronomical Society*, 342:422–426, June 2003.

[41] K. N. P. M. O. I. M. G. J. N. Reeves. An xmmnewton survey of broad iron lines in seyfert galaxies. *Monthly Notices of the Royal Astronomical Society*, 382:194–228, Nov. 2007.

[42] H. N. Rivay Mor and M. Elitzur. Dusty structure around type-i active galactic nuclei: Clumpy torus narrow line region and near-nucleus hot dust. *Astrophysics Journal*, 705:298–313, 07 2009.

[43] D. J. A. S.W. Unger, A. Pedlar. The extended narrow-line region in radio seyferts: evidence for a collimated nuclear uv field? *Monthly Notices of the Royal Astronomical Society*, 228:671–679, 10 1987.

[44] L. M. Turner and J. Reeves. An absorption origin for the x-ray spectral variability of mcg6-30-15. *The Astrophysics and Astronomy journal*, 483:437–452, 05 2008.

[45] UCSD. Mrk 110 data from RXTE. `https://cass.ucsd.edu/~rxteagn/Mkn110/Mkn110.html`, Oct, 2013. [Online;].

[46] K. W. Accretion disk wind in the agn broad-line region: Spectroscopically resolved line profile variations in mrk 110. *Astronomy and AStrophysics*, 407:461–472, August 2003.

[47] K. W. Spin orientation of supermassive black holes in active galaxies. *Astronomy and AStrophysics*, 412:L61–L64, Dec. 2003.